Quantum theory of electrically levitated nanoparticle-ion systems: Motional dynamics and sympathetic cooling

Saurabh Gupta,[1] Dmitry S. Bykov,[2] Tracy E. Northup,[2] and Carlos Gonzalez-Ballestero[1, *]

[1]*Institute for Theoretical Physics, Technical University of Vienna,*
Wiedner Hauptstraße 8-10, 1040 Vienna, Austria
[2]*Institut für Experimentalphysik, Universität Innsbruck, Technikerstraße 25, 6020 Innsbruck, Austria*
(Dated: November 27, 2025)

We develop the theory describing the quantum coupled dynamics of the center-of-mass motion of a nanoparticle and an ensemble of ions co-trapped in a dual-frequency linear Paul trap. We first derive analytical expressions for the motional frequencies and classical trajectories of both nanoparticle and ions. We then derive a quantum master equation for the ion-nanoparticle system and quantify the sympathetic cooling of the nanoparticle motion enabled by its Coulomb coupling to a continuously Doppler-cooled ion. We predict that motional cooling down to sub-kelvin temperatures is achievable in state-of-the-art experiments even in the absence of motional feedback and in the presence of micromotion. We then extend our analysis to an ensemble of N ions, predicting a linear increase of the cooling rate as a function of N and motional cooling of the nanoparticle down to tenths of millikelvin in current experimental platforms. Our work establishes the theoretical toolbox needed to explore the ion-assisted preparation of non-Gaussian motional states of levitated nanoparticles.

I. INTRODUCTION

The preparation of macroscopic quantum states of the center-of-mass motion of nanoparticles levitated in high vacuum is a central goal in levitated optomechanics. Such states could, among others, shed light on the mechanisms behind the quantum-to-classical transition and enable tests of the quantum nature of gravity [1, 2]. Following demonstrations of ground-state motional cooling [3–9] and motional squeezing [10, 11] of an optically trapped nanoparticle, the next key milestone is the preparation of non-Gaussian motional states. However, for optically trapped nanoparticles, motional decoherence induced by laser recoil heating [12] remains a major obstacle. Proposed strategies to overcome this challenge rely on either switching off the trapping light [13–18] or implementing hybrid control schemes with electric and magnetic potentials [19–30].

An alternative route is to employ all-electrical traps in ultra-high vacuum [31–36], where nanoparticles can achieve record-low damping rates [37]. The recent demonstration of co-trapping a nanoparticle together with one or more ions [38] opens the door to leveraging the control capabilities of ion quantum optics for levitated optomechanics. For example, Doppler-cooled ions could be used to sympathetically cool the nanoparticle through their Coulomb interaction [39–41]. This possibility, which according to classical estimations is reachable in current setups [38], would relax the need to optically address the nanoparticle. Furthermore, the internal qubit transition of the ions could be directly used to prepare non-Gaussian motional states [42–44]. To fully harness these capabilities, however, a quantum theory of the coupled ion-nanoparticle dynamics is needed.

In this article we provide such quantum theory and quantify the nanoparticle motional temperatures reachable by ion-based sympathetic cooling. First, in Sec. II, we derive the secular motional frequencies of a nanoparticle and an ion in a dual-frequency linear Paul trap, their classical trajectories including the first motional sideband, and their quantum Hamiltonian. In Sec. III, we derive a master equation including the linearised Coulomb coupling between ion and nanoparticle as well as the common sources of dissipation in current experiments. We proceed in Sec. IV by computing analytically the steady-state occupations of the nanoparticle motional degrees of freedom under continuous Doppler cooling of the ion, as well as the corresponding ion-induced motional cooling rates. We also extend our analysis by including the effect of micromotion. We extend this formalism to multiple ions in Sec. V. Finally, our conclusions are presented in Sec. VI.
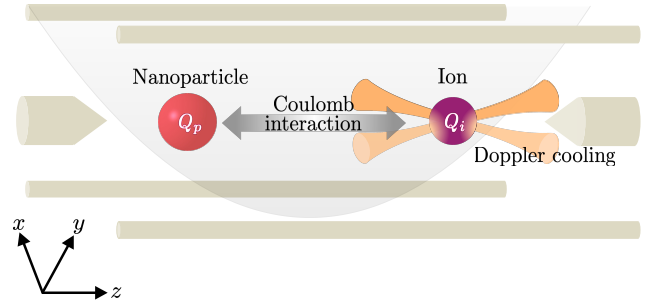

FIG. 1. Scheme of the system under study. A charged dielectric nanoparticle is co-trapped with a single or multiple ions in a two-tone Paul trap. The center-of-mass motion of the nanoparticle is coupled to the ion motion by Coulomb interaction. The ion motion can be continuously Doppler-cooled using laser beams.

* carlos.gonzalez-ballestero@tuwien.ac.at

II. DYNAMICS OF A CHARGED PARTICLE IN A DUAL-FREQUENCY TRAP

The system under study, schematically depicted Fig. 1, consists on a spherical dielectric nanoparticle with charge Q_p, radius R_p, and mass M_p, and an ion with charge Q_i and mass M_i. Both the nanoparticle and ion lie near the center of a linear Paul trap and interact via Coulomb forces. The geometric center of the trap is chosen as the origin of coordinates, with the endcap electrodes lying along the $z-$axis and the four axial electrodes intersecting either the $x-$ or the $y-$axis. Throughout this work we will consider a two-tone Paul trap, i.e., a trap where two AC voltages with different frequencies are applied to the electrodes. These two tones are necessary in order to trap two objects with very different charge-to-mass ratios [45–47]. Finally, we assume that the center of charge of the nanoparticle coincides with its center of mass, so that the motional and rotational dynamics decouple. In this section we describe the independent classical and quantum dynamics of each individual particle, as a key step to describe their coupled quantum dynamics in subsequent sections. First, we determine the secular frequencies and classical motional trajectories of the nanoparticle and ion in a dual-frequency Paul trap in Sec. II A. Then, in Sec. II B, we use these results to derive their quantum Hamiltonian.

A. Classical dynamics in the two-tone Paul trap

To derive the free quantum motional Hamiltonians of the ion and the nanoparticle, we first need to solve their classical dynamics [50]. We thus consider a single particle with charge Q and mass M in the two-tone Paul trap described above. For the sake of generality, in this section we assume a generic configuration of the trap in which there is a static as well as a time-dependent potential along each axis. The total electric potential experienced by a charged particle at position $\mathbf{R}$ near the center of the trap is given by [50, 51]

$$\phi\left(\boldsymbol{R}, t\right) = \sum_{j=x,y,z} \frac{R_j^2}{2d_j^2}$$
$$\times \left(U_{0j} + U_{sj}\cos\left(\omega_s t\right) + U_{fj}\cos\left(\omega_f t\right)\right)\alpha_j, \quad (1)$$

where U_{0j}, U_{sj}, and U_{fj} are the amplitudes of the static, slow-oscillating, and fast-oscillating voltages applied to the electrode at axis $j(=x,y,z)$. The slow and fast voltages oscillate at frequencies ω_s and ω_f respectively. The geometry of the trap is encoded in the parameters d_j, namely the distance between the electrodes at axis j and the trap center, and the geometric factor α_j that accounts for deviations from a perfect quadrupole trap (for which $\alpha_j = 1$). The trap parameters fulfill the constraint

$$\sum_{j=x,y,z} \frac{U_{0j}\alpha_j}{d_j^2} = \sum_{j=x,y,z} \frac{U_{sj}\alpha_j}{d_j^2} = \sum_{j=x,y,z} \frac{U_{fj}\alpha_j}{d_j^2} = 0, \quad (2)$$

due to Gauss' divergence law.

Since the potential Eq. (1) is separable, the dynamics of the particle along each axis are decoupled, and obey the equation

$$\frac{\mathrm{d}^2 R_j}{\mathrm{d}t^2} + \frac{Q\alpha_j}{Md_j^2}\Big(U_{0j} +$$
$$+ U_{sj}\cos\left(\omega_s t\right) + U_{fj}\cos\left(\omega_f t\right)\Big)R_j = 0. \quad (3)$$

It is convenient to write the above equation in dimensionless form by rescaling time to the fast radiofrequency (RF) tone as $\tau \equiv \omega_f t/2$. We obtain the two-tone Mathieu equation

$$\frac{\mathrm{d}^2 R}{\mathrm{d}\tau^2} + \left(a + 2q_s l^2 \cos\left(2l\tau\right) + 2q_f \cos\left(2\tau\right)\right)R = 0, \quad (4)$$

where hereafter we drop the index j for simplicity. In the above expression we have defined the ratio between slow and fast frequencies, $l \equiv \omega_s/\omega_f$, and the parameters

$$\begin{bmatrix} a \\ q_s \\ q_f \end{bmatrix} \equiv \frac{2Q}{Md^2\omega_f^2} \begin{bmatrix} 2U_0\alpha \\ U_s\alpha/l^2 \\ U_f\alpha \end{bmatrix}. \quad (5)$$

For certain regimes of values of the above parameters, Eq. (4) admits quasi-harmonic solutions, namely solutions that oscillate at a frequency much smaller than ω_f – the secular frequency – with small contributions that oscillate at the RF frequencies, also referred to as micromotion. Our goal is to obtain approximate expressions for these stable solutions as well as for the secular frequencies in the experimentally relevant regime $a, q_s^2 l^4, q_f^2 \ll 1$.

1. Secular frequencies

We first start by determining the secular frequencies. Note that, to trap objects with such different charge-to-mass ratios as an ion and a ~ 100 nm nanoparticle, the two RF frequencies must be very different [38], i.e., $\omega_s \ll \omega_f$, or equivalently $l \ll 1$. We make use of the modified Lindstedt-Poincaré method [52, 53] to compute the secular frequency in this regime as a perturbative expansion in the parameters $q_s l^2$ and q_f. We will hereafter assume that the trap voltages fulfill $U_s < U_f$ so that one of the two perturbation parameters is at most of the same order as the second, $q_s l^2 = (U_s/U_f)q_f \lesssim q_f$. This allows us to expand in the single parameter q_f.

The starting point of the modified Lindstedt-Poincaré method is to assume that the solution of Eq. (4), $R(\tau)$, oscillates at a dimensionless secular frequency β, i.e. $R(\tau) \approx \exp(i\beta\tau)$, that can be perturbatively expanded as

$$\beta^2 = a - \sum_{n=1}^{\infty} q_f^n \beta_{(n)}. \quad (6)$$

TABLE I. System parameters used as case study. These parameters correspond to the experiment in Ref. [38].

Parameter	Description	Value
R_p	Nanoparticle radius	134×10^{-9} m
M_p	Nanoparticle mass	2.0×10^{-17} kg
Q_p	Nanoparticle charge	$750 \times 1.6 \times 10^{-19}$ C
M_i	Ion mass	$40 \times 1.6 \times 10^{-27}$ kg
Q_i	Ion charge	1.6×10^{-19} C
$[d_x, d_y, d_z]$	Distance between electrode and trap center	$[0.9, 0.9, 1.7]$ mm
$[\alpha_x, \alpha_y, \alpha_z]$	Geometric factor	$[0.93, 0.93, 0.38]$
$[U_{0x}, U_{0y}, U_{0z}]$	Static voltage	$[3.2, 3.2, 56.5]$ V
$[U_{sx}, U_{sy}, U_{sz}]$	Slow RF voltage	$[80, -80, 0]$ V[a]
ω_s	Slow frequency	$2\pi \times 7$ kHz
$[U_{fx}, U_{fy}, U_{fz}]$	Fast RF voltage	$[1.35, -1.35, 0]$ kV[a]
ω_f	Fast frequency	$2\pi \times 17.5$ MHz
T	Temperature of surrounding gas	300 K
P	Pressure of surrounding gas	7×10^{-11} mbar
$\dot{E}^{\mathrm{dop}}$	Energy heating rate of the ion due to photon recoil	3.8×10^{-22} J/s
γ^{dop}	Doppler cooling rate of the ion	$2\pi \times 10$ kHz
$[\Omega_{xp}, \Omega_{yp}, \Omega_{zp}]$	Mechanical frequencies of nanoparticle	$2\pi \times [1.59, 1.19, 1.06]$ kHz
$[\Omega_{xi}, \Omega_{yi}, \Omega_{zi}]$	Mechanical frequencies of ion	$2\pi \times [3.96, 3.90, 0.68]$ MHz
$\boldsymbol{D_i} - \boldsymbol{D_p}$	Nanoparticle-ion equilibrium separation	$[0, 0, 52.58]$ μm
γ^{gas}	Damping rate of the nanoparticle due to surrounding gas	$2\pi \times 44.5$ nHz
$\dot{E}^{\mathrm{td}}$	Energy heating rate of the nanoparticle due to trap-displacement noise	2.8×10^{-26} J/s

[a] Note that we neglected the RF field contribution along the z-axis, as it can be minimized experimentally using a symmetric trap drive [48] or a linear Paul trap with RF electrode spacing much smaller than that of the end-cap electrodes. In the former, the RF null along the entire trap axis is achieved by driving two RF electrode pairs with equal amplitude and frequency, but phase-shifted by π. In the latter, the RF field is zero at only one point on the z-axis but remains weak away from this point, minimally affecting the dynamics of the trapped objects. For example, this configuration is used in state-of-the-art trapped-ion quantum information processing experiments without compromising qubit operations mediated by collective ion motion [49].

Similarly, the displacement can also be expanded in orders of q_f as

$$R(\tau) = \sum_{n=0}^{\infty} q_f^n R_{(n)}(\tau). \qquad (7)$$

We then introduce Eqs. (6-7) into Eq. (4) and isolate the terms of the same order in q_f into independent equations. Each of them is a differential equation for $R_{(n)}(\tau)$ which depends on lower order terms $R_{(n)}(\tau), R_{(n-1)}(\tau), ...R_{(0)}(\tau)$, providing a recursive method to compute the solution up to the desired order in q_f. Since the solution $R(\tau)$ is stable by assumption, any resonant driving terms $\propto \exp(\pm i\beta\tau)$ appearing in each of these equations must cancel. This condition fixes the values of the coefficients $\beta_{(n)}$. We include terms up to second order in q_f in Eq. (6), obtaining the following equation for the dimensionless frequency β,

$$\beta^2 = a + \frac{q_f^2}{2} + \frac{q_s^2 l^4}{2\left(l^2 - \beta^2\right)}. \qquad (8)$$

In deriving the above expression we have used the fact that in the regime of interest $a, q_f^2 \ll 1$, the dimensionless

secular frequency must also be small, $\beta^2 \ll 1$. The true secular frequency is given by $\Omega = \beta\omega_f/2$. Note that in the limit of a single-frequency Paul trap, $l \to 0$, Eq. (8) recovers the well-known expression [50]

$$\lim_{l\to 0} \Omega = \Omega_f \equiv \frac{\omega_f}{2}\sqrt{a + q_f^2/2}. \qquad (9)$$

The solution of Eq. (8) strongly depends on the parameters of the Mathieu equation, and is thus different for the nanoparticle and the ion. For the nanoparticle, whose charge-to-mass ratio is much smaller than of the ion, the condition $a, q_f^2, q_s^2 l^4 \ll l^2$ is typically fulfilled. In this regime of parameters one has $\beta^2 \ll l^2$ (see Eq. (6)) and the solution to Eq. (8) simplifies to $\beta^2 \approx a + (q_f^2/2) + (q_s^2 l^2/2)$. The nanoparticle secular frequency can thus be approximated as

$$\Omega_p \approx \sqrt{\frac{Q_p U_0 \alpha}{M_p d^2} + \frac{1}{2}\left(\frac{Q_p \alpha}{M_p d^2}\right)^2\left(\frac{U_s^2}{\omega_s^2} + \frac{U_f^2}{\omega_f^2}\right)}. \qquad (10)$$

Note that the nanoparticle frequency is dominated by the contribution from the slow RF signal. In the case of the ion, the above simplifications are typically not possible

and Eq. (8) needs to be fully solved. The ion secular frequency thus reads [54]

$$\Omega_i \approx \frac{1}{\sqrt{2}} \left(\Omega_f^2 + \frac{\omega_s^2}{4} + \right.$$
$$\left. + \sqrt{\left(\Omega_f^2 - \frac{\omega_s^2}{4} \right)^2 - \frac{Q_i^2 U_s^2 \alpha^2}{2 M_i^2 d^4}} \right)^{1/2}. \quad (11)$$

The secular frequencies predicted by Eqs. (10) and (11), shown in Table I for parameters of Ref. [24], quantitatively reproduce experimental observations. Note that, due to the asymmetry of trap parameters, the mechanical frequencies along each axis are different.

2. Displacement functions

The Lindstedt-Poincaré method is especially suited to compute secular frequencies, as it allows to capture terms of all orders in the perturbative parameter q_f (see e.g. Eq. (9)). This is not true for the computed displacement function $R(\tau)$, which remains a finite-order expansion and thus less accurate than the Floquet solutions obtained in single-frequency traps. To derive a solution with similar level of accuracy, we employ a modified Dehmelt approximation [55]. First, we assume the following Ansatz for the solution of Eq. (4) in the regime $a, q_f^2 \ll 1$,

$$R(\tau) = e^{i\beta\tau} \left(u_0 + u_s(\tau) + u_f(\tau) \right), \quad (12)$$

where u_0 is a constant of order 1 and $u_s(\tau), u_f(\tau) \sim O(q_f)$ are slow and fast oscillating solutions at frequencies of order $2l$ and 2, respectively. We do not fix a specific value for β but assume it to be small, $\beta \ll 1$. This condition is fulfilled for both the nanoparticle and the ion for the parameters given in Table I, as shown in the previous section.

Introducing Eq. (12) into Eq. (4), we obtain

$$\ddot{u}_f + \ddot{u}_s + 2i\beta(\dot{u}_f + \dot{u}_s) + (a - \beta^2 + 2q_f \cos(2\tau) + 2q_s l^2 \cos(2l\tau))(u_0 + u_s + u_f) = 0. \quad (13)$$

We proceed by isolating the terms oscillating at the fast frequency into a single equation, where we neglect all terms of order aq_f, q_f^2, or $\beta^2 q_f$. The resulting approximate equation for $u_f(\tau)$ has the solution

$$u_f(\tau) \approx \frac{q_f}{2} \cos(2\tau) u_0, \quad (14)$$

to lowest order in a, q_f^2. We now introduce this solution into Eq. (13) and take a time average over one period of the fast frequency, assuming that all functions which

oscillate at the slow frequency remain approximately constant within such period. We obtain

$$\ddot{u}_s + 2i\beta\dot{u}_s + \frac{q_f^2 u_0}{2(1 - \beta^2)} + + (a - \beta^2 + 2q_s l^2 \cos(2l\tau))(u_0 + u_s) = 0. \quad (15)$$

Repeating the above steps for the slow timescale we obtain the following expression for the slowly varying amplitude,

$$u_s(\tau) \approx \frac{q_s l^2}{2(l^2 - \beta^2)} \cos(2l\tau) u_0. \quad (16)$$

We also obtain with this method the same equation for the secular frequencies that we derived through the modified Lindstedt-Poincaré method, Eq. (8). This confirms the consistency of our secular frequency calculation.

Combining Eqs. (12), (14), and (16), we obtain an expression for the displacement up to a multiplicative constant u_0. We fix this constant by imposing the initial conditions $R(0) = 1$ and $\dot{R}(0) = i\beta$, a convenient choice to write the quantum Hamiltonian as we will see below. The final displacement in real time reads

$$R(t) = e^{i\Omega t} \left(1 + \frac{q_f}{2} + \frac{q_s l^2}{2(l^2 - \beta^2)} \right)^{-1}$$
$$\times \left(1 + \frac{q_f}{2} \cos(\omega_f t) + \frac{q_s l^2}{2(l^2 - \beta^2)} \cos(\omega_s t) \right), \quad (17)$$

where Ω is the secular frequency given in Eqs. (10-11). Note that in the limit $l \to 0$ the above equation recovers the well-known expression for single-frequency traps [50]. Note also that the solution Eq. (17) is consistent with the initial assumptions – specifically, the assumption of $u_s(\tau)$ being small – only if

$$\frac{q_s l^2}{2(l^2 - \beta^2)} \ll 1. \quad (18)$$

This condition is fulfilled for the parameters of Table I and will be assumed to hold hereafter.

B. Quantum Hamiltonian of a particle in the two-tone Paul trap

The Hamiltonian describing the dynamics of a particle along one of the Cartesian axes of the Paul trap is given in the Schrödinger picture by [50]

$$\hat{H}(t) = \frac{\hat{P}^2}{2M} + \frac{M}{2} W(t) \hat{R}^2, \quad (19)$$

with $\hat{R}$ and $\hat{P}$ the position and momentum operators along the chosen axis, and

$$W(t) \equiv \frac{\omega_f^2}{4} \left(a + 2q_s l^2 \cos(\omega_s t) + 2q_f \cos(\omega_f t) \right). \quad (20)$$

Note that the function $W(t)$ is different for each of the three axes. In the following, Heisenberg picture operators are denoted by the superindex (H).

Since the Heisenberg picture position operator $\hat{R}^{(H)}(t)$ satisfies the two-tone Mathieu equation Eq. (4), we can combine it with the scalar solution obtained above, $R(t)$, into the operator [50]

$$\hat{C}^{(H)}(t) \equiv \sqrt{\frac{M}{2\hbar\Omega}} i \left(R(t)\dot{\hat{R}}^{(H)}(t) - \dot{R}(t)\hat{R}^{(H)}(t) \right), \quad (21)$$

which is by definition time-independent, $\hat{C}^{(H)}(t) = \hat{C}^{(H)}(0)$. Introducing the initial conditions $R(0) = 1$ and $\dot{R}(0) = i\Omega$ we can write this operator as a Schrödinger picture ladder operator for a harmonic oscillator with the secular frequency Ω, i.e.,

$$\hat{C}^{(H)}(t) = \sqrt{\frac{M}{2\hbar\Omega}} i \left(\frac{\hat{P}^{(H)}(0)}{M} - i\Omega\hat{R}^{(H)}(0) \right) \equiv \hat{b}. \quad (22)$$

Combining Eqs. (21-22) and their complex conjugates we can reexpress the position and momentum operators as

$$\hat{R}^{(H)}(t) = \sqrt{\frac{\hbar}{2M\Omega}} \left(\hat{b}R^*(t) + \hat{b}^\dagger R(t) \right), \quad (23)$$

$$\hat{P}^{(H)}(t) = \sqrt{\frac{\hbar M\Omega}{2}} \left(\hat{b}\frac{\dot{R}^*(t)}{\Omega} + \hat{b}^\dagger\frac{\dot{R}(t)}{\Omega} \right). \quad (24)$$

Substituting these expressions into the Heisenberg picture Hamiltonian, we obtain

$$\hat{H}^{(H)}(t) = \frac{\hbar}{4\Omega} \left(\hat{b}\boldsymbol{v}^*(t) + \text{H.c.} \right)^2, \quad (25)$$

where we have defined the vector

$$\boldsymbol{v}(t) \equiv \left[\dot{R}(t), R(t)\sqrt{W(t)} \right]^T. \quad (26)$$

In the regime of interest $a, q_f \ll 1$, the above Hamiltonian can be simplified by introducing the solution Eq. (17) and undertaking a series of rotating wave approximations to eliminate all time-dependent terms. The Hamiltonian thus simplifies to that of a harmonic oscillator at the secular frequency,

$$\hat{H}^{(H)}(t) \approx \hat{H} = \hbar\Omega\hat{b}^\dagger\hat{b}. \quad (27)$$

The validity conditions of the rotating wave approximations are involved in general, but can be simplified in the case $\beta^2 \ll l^2$, which is typically fulfilled by the nanoparticle, and in the case $l^2 \ll \beta^2$, which is typically fulfilled by the ion. Specifically, the approximate Hamiltonian Eq. (27) is valid for the nanoparticle provided that $q_f\omega_f, q_s\omega_s \ll 16\Omega$, and for the ion provided that $q_f\omega_f \ll 16\Omega$ and $(q_s/64)(\omega_s/\Omega)^3|1 - (q_s/8)^2(\omega_s/\Omega)^2| \ll 1$. All these conditions are fulfilled for the parameters in Table I.

III. COUPLED QUANTUM DYNAMICS OF ION AND NANOPARTICLE

The coupled quantum dynamics of the motional degrees of freedom of ion and nanoparticle can be described by the quantum master equation

$$\dot{\hat{\rho}} = -\frac{i}{\hbar} \left[\hat{H}_i + \hat{H}_p + \hat{V}_{ip}, \hat{\rho} \right] + \mathcal{D}_p(\hat{\rho}) + \mathcal{D}_i(\hat{\rho}). \quad (28)$$

Here, $\hat{\rho}$ is the density matrix of the nanoparticle and ion motional degrees of freedom. The free motional Hamiltonians of nanoparticle and ion, $\hat{H}_i$ and $\hat{H}_p$, can be written using Eq. (27) as

$$\hat{H}_\sigma = \frac{\hat{\mathbf{P}}_\sigma^2}{2M_\sigma} + \frac{M_\sigma}{2} \sum_{j=x,y,z} \Omega_{j\sigma}^2 \hat{R}_{j\sigma}^2, \quad (29)$$

for for $\sigma = i, p$, with $\Omega_{j\sigma}$ the secular frequency along axis j and with $\hat{\boldsymbol{R}}_\sigma = [\hat{R}_{x\sigma}, \hat{R}_{y\sigma}, \hat{R}_{z\sigma}]$ and $\hat{\boldsymbol{P}}_\sigma = [\hat{P}_{x\sigma}, \hat{P}_{y\sigma}, \hat{P}_{z\sigma}]$ the respective position and momentum operators, fulfilling $[\hat{R}_{j\sigma}, \hat{P}_{j'\sigma'}] = i\hbar\delta_{jj'}\delta_{\sigma\sigma'}$. The term $\hat{V}_{ip}$ in Eq. (28) represents the Coulomb coupling between ion and nanoparticle, whereas the second and third terms describe the dissipative dynamics. In this section we discuss in detail the form of each of these terms. First, in Sec. III A, we linearize the Coulomb interaction, determine the equilibrium ion and nanoparticle positions, and compute their motional coupling rates. Then, in Sec. III B, we describe the terms contributing to the dissipative dynamics of ion and nanoparticle.

A. Coulomb interaction

Both nanoparticle and ion are charged and thus interact via electrostatic forces. Assuming the ion-nanoparticle separation is much larger than the diameter of the nanoparticle, their classical interaction energy is given by the Coulomb expression for point charges,

$$V_{ip} = \frac{1}{4\pi\varepsilon_0} \frac{Q_i Q_p}{|\boldsymbol{R}_i - \boldsymbol{R}_p|}. \quad (30)$$

We assume $Q_i Q_p > 0$ so that the forces are repulsive. The combination of Coulomb repulsion and the restoring force exerted by the electrodes determines the equilibrium positions of ion and nanoparticle within the trap, which will in general not be at the origin of coordinates. The equilibrium positions, which we denote by $\boldsymbol{D}_\sigma \equiv [d_{x\sigma}, d_{y\sigma}, d_{z\sigma}]^T$, are determined as the points where all forces vanish,

$$\left(M_\sigma \Omega_{j\sigma}^2 R_{j\sigma} + \frac{\partial}{\partial R_{j\sigma}} V_{ip} \right)_{\boldsymbol{R}_i = \boldsymbol{D}_i, \boldsymbol{R}_p = \boldsymbol{D}_p} = 0. \quad (31)$$

This condition forms a system of 6 nonlinear equations which can have multiple solutions. For two trapped objects – e.g. one nanoparticle and one ion – all these

solutions correspond to both objects lying along the same coordinate axes. The solution where both objects lie along the $z-$axis is given by $d_{x\sigma} = d_{y\sigma} = 0$ and $d_{zp} = -d_{zi}M_i\Omega_{zi}^2/(M_p\Omega_{zp}^2) = D(1 + M_p\Omega_{zp}^2/(M_i\Omega_{zi}^2))^{-1}$ with D being the total distance between ion and nanoparticle,

$$D \equiv |\boldsymbol{D}_i - \boldsymbol{D}_p| = \sqrt[3]{\frac{Q_iQ_p}{4\pi\varepsilon_0}\left(\frac{1}{M_p\Omega_{zp}^2} + \frac{1}{M_i\Omega_{zi}^2}\right)}. \quad (32)$$

Solutions along the $x-$ and $y-$axes have the same form as the above under exchange of indices $z \leftrightarrow x$ or $z \leftrightarrow y$. We remark that some of these solutions might correspond to local maxima of the potential in coordinate space and thus to unstable equilibria. Stability of the solutions is discussed below.

We quantise the Coulomb energy Eq. (30) by promoting the position variables to operators, $\mathbf{R}_\sigma \rightarrow \hat{\mathbf{R}}_\sigma$. Since we are interested in dynamics near equilibrium positions, we linearise the Coulomb interaction around them. We first write the displacement operators as

$$\hat{R}_{j\sigma} = d_{j\sigma} + \delta\hat{R}_{j\sigma}. \quad (33)$$

The new operators $\delta\hat{R}_{j\sigma}$ have the same canonical momenta $\hat{P}_{j\sigma}$ and describe displacements from the equilibrium position. They are assumed small, i.e., $\langle\delta\hat{R}_{j\sigma}\delta\hat{R}_{j'\sigma'}\rangle(t) \ll D^2$, so that the Coulomb interaction can be well approximated by its second-order Taylor expansion in the six variables $\delta\hat{R}_{j\sigma}/D$. Under this approximation the total ion-nanoparticle Hamiltonian becomes quadratic and can be compactly written as

$$\hat{H}_{\text{tot}} \equiv \hat{H}_i + \hat{H}_p + \hat{V}_{ip} \approx \frac{1}{2}\hat{\boldsymbol{P}}^T\bar{M}\hat{\boldsymbol{P}} + \frac{1}{2}\hat{\boldsymbol{X}}^T\bar{V}\hat{\boldsymbol{X}}. \quad (34)$$

Here, we have discarded constant terms and defined the compound variable vectors

$$\hat{\boldsymbol{X}} \equiv [\delta\hat{R}_{xi}, \delta\hat{R}_{yi}, \delta\hat{R}_{zi}, \delta\hat{R}_{xp}, \delta\hat{R}_{yp}, \delta\hat{R}_{zp}]^T, \quad (35)$$

and

$$\hat{\boldsymbol{P}} \equiv [\hat{P}_{xi}, \hat{P}_{yi}, \hat{P}_{zi}, \hat{P}_{xp}, \hat{P}_{yp}, \hat{P}_{zp}]^T, \quad (36)$$

the diagonal matrix of inverse masses,

$$\bar{M} \equiv \begin{bmatrix} M_i^{-1}\mathbb{1}_{3\times3} & \mathbb{0}_{3\times3} \\ \mathbb{0}_{3\times3} & M_p^{-1}\mathbb{1}_{3\times3} \end{bmatrix}, \quad (37)$$

and the generalised potential matrix

$$\bar{V} \equiv \begin{bmatrix} -\bar{N}_{\text{coul}} & \bar{N}_{\text{coul}} \\ \bar{N}_{\text{coul}} & -\bar{N}_{\text{coul}} \end{bmatrix} + \begin{bmatrix} \bar{V}_{di} & \mathbb{0}_{3\times3} \\ \mathbb{0}_{3\times3} & \bar{V}_{dp} \end{bmatrix}, \quad (38)$$

with $\bar{V}_{di} \equiv M_i\text{diag}[\Omega_{xi}^2, \Omega_{yi}^2, \Omega_{zi}^2]$, $\bar{V}_{dp} \equiv M_i\text{diag}[\Omega_{xi}^2, \Omega_{yi}^2, \Omega_{zi}^2]$, and

$$\bar{N}_{\text{coul}} \equiv \frac{Q_iQ_p}{4\pi\varepsilon_0 D^3}\left[\mathbb{1}_{3\times3} - 3\frac{(\boldsymbol{D}_i - \boldsymbol{D}_p)\otimes(\boldsymbol{D}_i - \boldsymbol{D}_p)}{D^2}\right] \quad (39)$$

with $x \otimes y$ denoting the Kronecker product.

1. Stability and coupling rates

The potential matrix Eq. (38) is in general not diagonal, resulting in coupling between the motional degrees of freedom. The diagonal terms of $\bar{V}$ describe the new motional frequencies, which are renormalised due to Coulomb interaction. These new frequencies read

$$\Omega_{j\sigma}^{'2} \equiv \Omega_{j\sigma}^2 + \frac{Q_iQ_p}{4\pi\varepsilon_0 M_\sigma D^3}\left(3\frac{(d_{ji} - d_{jp})^2}{D^2} - 1\right). \quad (40)$$

Both the frequency renormalisations and the motional couplings induced by Coulomb interaction can result in the Hamiltonian for the chosen equilibrium positions $\boldsymbol{D}_i$ and $\boldsymbol{D}_p$ to not be dynamically stable, even if the uncoupled dynamics of ion and nanoparticle are. A quadratic Hamiltonian – both classical and quantum – is dynamically stable if the matrix

$$\bar{K} \equiv \begin{bmatrix} \mathbb{0}_{6\times6} & -\mathbb{1}_{6\times6} \\ \mathbb{1}_{6\times6} & \mathbb{0}_{6\times6} \end{bmatrix}\begin{bmatrix} \bar{M} & \mathbb{0}_{6\times6} \\ \mathbb{0}_{6\times6} & \bar{V} \end{bmatrix} \quad (41)$$

is diagonalisable and has purely imaginary eigenvalues [56, 57]. Hereafter we focus on equilibria that fulfill the above stability criterion. We remark that this criterion only establishes stability of the secular solutions of the nanoparticle and ion dynamics, but the full solution of the dynamics including micromotion can still be unstable. For the results of this work full stability has also been confirmed through a more stringent stability criterion based on Floquet theory, which is introduced in Sec. IV B.

As discussed above, all the equilibrium configurations correspond to ion and nanoparticle lying along the same Cartesian axis. In such case the matrix $\bar{N}_{\text{coul}}$ is diagonal, simplifying the dynamics in two ways. First, the motional degrees of freedom of the ion along each Cartesian axis are uncoupled from each other, and the same occurs for the nanoparticle. Second, the only interactions between ion and nanoparticle are of the form $\sim \hat{R}_{ji}\hat{R}_{jp}$ for $j = x, y, z$, i.e., only the motional degrees of freedom along the same axis couple to each other. As a result the system can be decomposed into three decoupled subsystems, each formed by two harmonic oscillators. We use this result in the following sections to obtain analytical expressions for the steady-state expectation values.

To compute the motional coupling rates between ion and nanoparticle we define adimensional position and momentum quadratures,

$$\delta\hat{R}_{j\sigma} \equiv R_{j\sigma}^{\text{zpf}}\hat{q}_{j\sigma} \equiv \sqrt{\frac{\hbar}{2M_\sigma\Omega_{j\sigma}'}}\hat{q}_{j\sigma}, \quad (42)$$

$$\hat{P}_{j\sigma} \equiv P_{j\sigma}^{\text{zpf}}\hat{p}_{j\sigma} \equiv \sqrt{\frac{\hbar M_\sigma\Omega_{j\sigma}'}{2}}\hat{p}_{j\sigma}, \quad (43)$$

where $R_{j\sigma}^{\text{zpf}}$ and $P_{j\sigma}^{\text{zpf}}$ are the zero-point displacement and momentum in the renormalised harmonic trap, respectively. The newly defined operators commute as

$[\hat{q}_{j\sigma}, \hat{p}_{j'\sigma'}] = 2i\delta_{jj'}\delta_{\sigma\sigma'}$. In terms of these operators the Hamiltonian Eq. (34) reads

$$\hat{H}_{\text{tot}} = \sum_{\substack{j=x,y,z \\ \sigma=i,p}} \frac{\hbar\Omega'_{j\sigma}}{4} \left(\hat{q}_{j\sigma}^2 + \hat{p}_{j\sigma}^2\right) + \sum_{j=x,y,z} \hbar g_j \hat{q}_{ji}\hat{q}_{jp}, \quad (44)$$

where the coupling rates are given by

$$g_z = -\frac{1}{2\pi\varepsilon_0} \frac{Q_i Q_p}{D^3} \frac{R_{zi}^{\text{zpf}} R_{zp}^{\text{zpf}}}{\hbar}, \quad (45)$$

$$g_j = \frac{1}{4\pi\varepsilon_0} \frac{Q_i Q_p}{D^3} \frac{R_{ji}^{\text{zpf}} R_{jp}^{\text{zpf}}}{\hbar}, \quad (j = x, y). \quad (46)$$

Fig. 2 shows the total equilibrium separation between ion and nanoparticle, D, as well as the radial and longitudinal coupling rates Eqs. (45-46), as a function of nanoparticle charge and mass. We use the experimentally relevant parameters of Table I and focus on the equilibrium configuration where both nanoparticle and ion lie along the $z-$axis, which for these parameters is the only dynamically stable equilibrium. As shown in Fig. 2(a), D increases with nanoparticle charge as the stronger Coulomb repulsion pushes ion apart from nanoparticle. As a consequence, the coupling rates are decreasing functions of charge Q_p. At low values of charge, the renormalised motional frequency (Eq. (40)) along the $y-$axis approaches zero and the coupling rate g_y (given by Eq. (46)) sharply increases until, for $Q_p \lesssim 215$ e, the whole time-dependent Hamiltonian Eq. (19) becomes Floquet-unstable (see Sec. IV B for details). This instability threshold is marked with an open dot in Fig. 2. The separation D is practically constant with mass M_p within the range shown in Fig. 2(b), as it is dominated by the factor $(M_i\Omega_{zi})^{-2} \gg (M_p\Omega_{zp})^{-2}$ (see Eq. (32)). Within the mass range shown in the figure, the ion-nanoparticle coupling rates along the $x-$ and $z-$axis decrease with M_p due to the decrease in the zero-point fluctuations along these directions, $R_{jp}^{\text{zpf}} \sim (M_p + m_j)^{-1/4}$ (see Eqs. (10) and (40)) where we define the auxiliary constant $m_z = 0$ and $m_x = 7 \times 10^{-17}$ kg for the parameters of Table I. In contrast, the coupling rate along the $y-$axis increases with mass as the renormalised frequency along that axis becomes smaller. In analogy to the dependency with Q_p, at nanoparticle masses $M_p \approx 7 \times 10^{-17}$ kg (or equivalently radii $R_p \gtrsim 203$ nm) the coupled system becomes Floquet-unstable (open dot in Fig. 2(b)).

B. Dissipative dynamics

Let us finally describe the dissipative dynamics experienced by nanoparticle and ion, namely the general dissipators $\mathcal{D}_p(\hat{\rho})$ and $\mathcal{D}_i(\hat{\rho})$ in Eq. (28), respectively. The nanoparticle experiences three sources of dissipation,

$$\mathcal{D}_p(\hat{\rho}) = \sum_{j=x,y,z} \left(\mathcal{D}_{j,\text{gas}}(\hat{\rho}) + \mathcal{D}_{j,\text{fb}}(\hat{\rho}) + \mathcal{D}_{j,\text{td}}(\hat{\rho})\right). \quad (47)$$
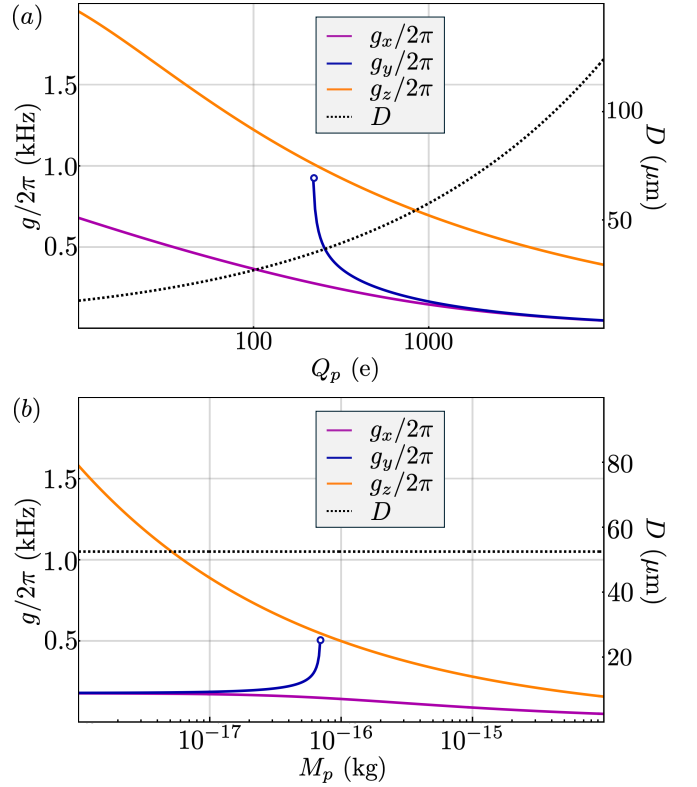

FIG. 2. Coupling rate between ion and nanoparticle center-of-mass motion along the $x-$ (Eq. (46), magenta), $y-$ (Eq. (46), blue), and $z-$axis (Eq. (45), orange) and equilibrium distance between the ion and nanoparticle (Eq. (32), dashed), versus nanoparticle charge Q_p (panel a) and nanoparticle mass M_p (panel b), for the parameters of Table I. The equilibrium position corresponds to nanoparticle and ion lying along the $z-$axis. The open dots mark the points beyond which the coupled system becomes unstable, see main text for details.

The first contribution is decoherence due to collisions with surrounding gas, modeled via the dissipator [58, 59]

$$\mathcal{D}_{j,\text{gas}}(\hat{\rho}) = -\frac{\Gamma_j^{\text{gas}}}{2} [\hat{q}_{jp}, [\hat{q}_{jp}, \hat{\rho}]]$$
$$- \frac{i\gamma^{\text{gas}}}{4} [\hat{q}_{jp}, \{\hat{p}_{jp}, \hat{\rho}\}], \quad (48)$$

where $\Gamma_j^{\text{gas}} \equiv \gamma^{\text{gas}} k_B T/(\hbar\Omega'_{jp})$ with k_B being Boltzmann's constant and T the temperature, and where the curly brackets denote the anti-commutator. The gas damping rate is given by [60, 61]

$$\gamma^{\text{gas}} = 0.619 \frac{6\pi R_p^2}{M_p} P \sqrt{\frac{2m_o}{\pi k_B T}}, \quad (49)$$

where P is the pressure of the surrounding gas and m_o is the molecular mass of the gas (which we fix to the mass of nitrogen molecules, $m_o = 4.65 \times 10^{-26}$ kg). At room temperature and the ultra-high vacuum pressures of typical experiments [37, 38], the condition $\gamma^{\text{gas}} k_B T \ll 2\hbar\Omega'_{jp}$ is fulfilled, allowing us to take a rotating wave

approximation and write the dissipator as

$$\mathcal{D}_{j,\text{gas}}(\hat{\rho}) \approx \left(\Gamma_j^{\text{gas}} + \gamma^{\text{gas}}\right)\mathcal{L}_{\hat{b}_{jp},\hat{b}_{jp}^\dagger}(\hat{\rho}) + \\ + \Gamma_j^{\text{gas}}\mathcal{L}_{\hat{b}_{jp}^\dagger,\hat{b}_{jp}}(\hat{\rho}), \quad (50)$$

where we define the Lindblad dissipator $\mathcal{L}_{\hat{a},\hat{b}}(\hat{\rho}) \equiv \hat{a}\hat{\rho}\hat{b} - \frac{1}{2}\{\hat{b}\hat{a},\hat{\rho}\}$, with $\hat{b}_{j\sigma} \equiv (\hat{q}_{j\sigma} + i\hat{p}_{j\sigma})/2$ being the ladder operators of the harmonic motion of particle $\sigma = i, p$ along the coordinate axis $j = x, y, z$.

The second term in Eq. (47) describes measurement-based feedback cooling of the nanoparticle, which is commonly employed to stabilise the nanoparticle in electrical levitation experiments [20, 22, 24–30, 32–34, 36, 37]. We assume the measurement is performed optically and thus model the effect of feedback through the dissipator

$$\mathcal{D}_{j,\text{fb}}(\hat{\rho}) = \gamma^{\text{fb}}\mathcal{L}_{\hat{b}_{jp},\hat{b}_{jp}^\dagger}(\hat{\rho}) - \frac{\Gamma_j^{\text{ba}}}{2}[\hat{q}_{jp},[\hat{q}_{jp},\hat{\rho}]]. \quad (51)$$

The first term describes motional damping at a rate γ^{fb}, which for simplicity we assume equal for all motional axes. The second term describes decoherence due to measurement backaction, i.e., recoil heating rate. Assuming the measurement is performed with a conventional Gaussian beam, the recoil heating rate reads $\Gamma_j^{\text{ba}} = \zeta(P_t/W_t^2)\alpha_p^2 k_0^5 (R_{jp}^{\text{zpf}})^2/(15\pi^2\hbar\varepsilon_0^2 c)$ where $\lambda_0 = 2\pi/k_0$, P_t, and W_t are the wavelength, power, and waist of the probing beam, c the speed of light, and where $\alpha_p = 4\pi\varepsilon_0 R_p^3(\varepsilon - 1)/(\varepsilon + 2)$ is the polarisability of the nanoparticle with ε its relative permittivity [59, 62]. The factor $\zeta \in \{1, 2, 7\}$ depends on the direction and polarisation of the optical probe beam with respect to the motional axis j. For ideal feedback, the damping rate is proportional to the light intensity at the nanoparticle position, i.e. we can write $\gamma^{\text{fb}} = c_{\text{fb}}P_t/W_t^2$ with c_{fb} a constant that depends on the specific experimental setup. This allows us to write the recoil heating rate as

$$\Gamma_j^{\text{ba}} = \zeta(\gamma^{\text{fb}}/c_{\text{fb}})\frac{\alpha_p^2 k_0^5 R_{jp}^{\text{zpf}2}}{15\pi^2\hbar\varepsilon_0^2 c}, \quad (52)$$

an expression that is convenient when particularizing to specific setups.

Finally, the third term in Eq. (47) describes additional trap-displacement noise,

$$\mathcal{D}_{j,\text{td}}(\hat{\rho}) = -\frac{\Gamma_j^{\text{td}}}{2}[\hat{q}_{jp},[\hat{q}_{jp},\hat{\rho}]]. \quad (53)$$

This noise can originate from various mechanisms (stray electromagnetic fields, noise in the voltage applied to the Paul trap electrodes, mechanical vibrations,...) and is the current dominant source of decoherence in electrical levitation experiments in high vacuum [37]. The rates are given by $\Gamma_j^{\text{td}} \equiv \dot{E}^{\text{td}}/(\hbar\Omega'_{jp})$ where the energy heating rate $\dot{E}^{\text{td}}$ is a free parameter of our model that can be fixed to experimental measurements.

We finally focus on the motional dissipative dynamics of the ion. We assume the ion is Doppler-cooled using laser beams such that the motional dissipation is dominated by the interaction with such beams, i.e.,

$$\mathcal{D}_i(\hat{\rho}) = \sum_{j=x,y,z}\left(\Gamma_j^{\text{dop}} + \gamma^{\text{dop}}\right)\mathcal{L}_{\hat{b}_{ji},\hat{b}_{ji}^\dagger}(\hat{\rho}) + \\ + \Gamma_j^{\text{dop}}\mathcal{L}_{\hat{b}_{ji}^\dagger,\hat{b}_{ji}}(\hat{\rho}). \quad (54)$$

Here, γ^{dop} is the Doppler cooling rate and $\Gamma_j^{\text{dop}} \equiv \dot{E}^{\text{dop}}/(\hbar\Omega'_{ji})$ is the heating rate due to recoil heating and residual excitation of blue sideband transitions [63], with $\dot{E}^{\text{dop}}$ being the energy heating rate.

This section concludes the derivation of the coupled motional dynamics of ion and nanoparticle. In the following sections we will use our derived master equation to explore ion-based sympathetic cooling of the nanoparticle center-of-mass motion.

IV. SYMPATHETIC COOLING

Electrically trapped nanoparticles have lower motional frequencies than their optically levitated counterparts, which reduces the effectiveness of motional cooling and hinders reaching the ground state. Trapped ions could help bridge this gap, as their motion can be Doppler-cooled at a fast rate. Since the motion of ion and nanoparticle are coupled via Coulomb interaction, continuously cooled ions can be used as energy sinks to remove thermal energy from the nanoparticle motion. In this section, we quantify this so-called sympathetic cooling. First, in Sec. IV A, we derive equations of motion for the system observables and compute the occupation of the nanoparticle center-of-mass motion in the presence of the ion. Then, in Sec. IV B, we quantify the impact of micromotion on sympathetic cooling.

A. Equations of motion and phonon occupations

Since the ion motion along axis j only couples to the nanoparticle motion along the same axis j as discussed above, the dynamics can be described by three independent subsystems of two coupled oscillators each. The dynamics of the expectation value of an arbitrary operator in one of these subsystems, $\hat{O}_j$, can be computed directly from the master equation Eq. (28),

$$\frac{\mathrm{d}\langle\hat{O}_j\rangle}{\mathrm{d}t} = -\frac{i}{\hbar}\text{Tr}\left[\left[\hat{O}_j,\hat{H}_{\text{tot}}\right]\hat{\rho}\right] + \\ + \text{Tr}\left[\hat{O}_j\left(\mathcal{D}_p(\hat{\rho}) + \mathcal{D}_i(\hat{\rho})\right)\right]. \quad (55)$$

Specifically, we derive the closed systems of equations

$$\frac{\mathrm{d}\langle\hat{\boldsymbol{B}}_j\rangle}{\mathrm{d}t} = \bar{A}_j\langle\hat{\boldsymbol{B}}_j\rangle, \quad (56)$$

and

$$\frac{\mathrm{d}}{\mathrm{d}t}\bar{\sigma}^j = \bar{A}_j \bar{\sigma}^j + \bar{\sigma}^j \bar{A}_j^T + \bar{C}_j, \qquad (57)$$

where we have defined the ladder operator vector as $\hat{\boldsymbol{B}}_j \equiv [\hat{b}_{ji}, \hat{b}_{ji}^\dagger, \hat{b}_{jp}, \hat{b}_{jp}^\dagger]^T$ and its covariance matrix as

$$\bar{\sigma}_{\lambda\mu}^j \equiv \frac{1}{2}\langle \hat{B}_{j\lambda}\hat{B}_{j\mu} + \hat{B}_{j\mu}\hat{B}_{j\lambda}\rangle - \langle\hat{B}_{j\lambda}\rangle\langle\hat{B}_{j\mu}\rangle, \qquad (58)$$

for $\lambda, \mu = 1, 2, 3, 4$. The 4×4 drift matrix $\bar{A}_j$ reads

$$\bar{A}_j \equiv \mathrm{diag}[-i\Omega'_{ji}, i\Omega'_{ji}, -i\Omega'_{jp}, i\Omega'_{jp}]+$$
$$+ \left[\begin{array}{c|c} -(\gamma^{\mathrm{dop}}/2)\mathbb{1}_{2\times 2} & -ig_j\mathbb{Z}\mathbb{J}_{2\times 2} \\ \hline -ig_j\mathbb{Z}\mathbb{J}_{2\times 2} & -((\gamma^{\mathrm{fb}}+\gamma^{\mathrm{gas}})/2)\mathbb{1}_{2\times 2} \end{array}\right], \quad (59)$$

where $\mathbb{Z}$ is the Pauli-Z matrix and $\mathbb{J}_{n\times n}$ is a $n \times n$ matrix whose entries are all equal to 1. The 4×4 diffusion matrix $\bar{C}_j$ reads

$$\bar{C}_j \equiv \begin{bmatrix} 0 & \Gamma_j^{\mathrm{dop}} & -ig_j & 0 \\ \Gamma_j^{\mathrm{dop}} & 0 & 0 & ig_j \\ -ig_j & 0 & \Gamma_j^{\mathrm{gas}} - \Gamma_{jp} & \Gamma_{jp} \\ 0 & ig_j & \Gamma_{jp} & \Gamma_j^{\mathrm{gas}} - \Gamma_{jp} \end{bmatrix}, \quad (60)$$

where we have defined the total nanoparticle heating rate, $\Gamma_{jp} \equiv \Gamma_j^{\mathrm{gas}} + \Gamma_j^{\mathrm{td}} + \Gamma_j^{\mathrm{ba}}$. From the covariance matrix $\bar{\sigma}^j$, we extract the steady-state phonon occupation of the nanoparticle along each direction $j = x, y, z$, i.e., $\langle \hat{n}_{jp}\rangle_{\mathrm{ss}} \equiv \langle \hat{b}_{jp}^\dagger \hat{b}_{jp}\rangle_{\mathrm{ss}}$. The full analytical expression of this occupation is given in Appendix A.

The steady-state phonon occupations along the z and the radial directions are shown in Fig. 3 for the parameters in Table I as a function of the total nanoparticle damping rate, $\gamma_p \equiv \gamma^{\mathrm{fb}} + \gamma^{\mathrm{gas}}$, for two values of the total heating rate Γ_{jp}. The blue and green lines mark two relevant values of the damping rate, namely the damping rate in the absence of feedback ($\gamma_p = \gamma^{\mathrm{gas}} = 2\pi \times 44.5$ nHz) and the typical damping rate achieved in state-of-the-art experiments [38] ($\gamma_p \approx \gamma^{\mathrm{fb}} = 2\pi \times 1$ Hz). The solid black curves in panels (a) and (b) correspond to the values of such experiment, where the nanoparticle heating is dominated by trap-displacement noise with rates $\Gamma_z^{\mathrm{td}} = 2\pi \times 6.3$ kHz and $\Gamma_x^{\mathrm{td}} = 2\pi \times 4.2$ kHz, respectively. This decoherence source, however, is not fundamental and can be significantly suppressed. The results for $\Gamma_j^{\mathrm{td}} = 0$ are shown by the dotted black line.

In general, the nanoparticle occupations in Fig. 3 are always lower than their room-temperature values (1.4×10^{11} and 5.9×10^9 in the $z-$axis and 9.6×10^{10} and 3.9×10^9 in the $x-$axis with and without trap-displacement noise, respectively), indicating motional cooling for all values of γ_p across two distinct regimes. First, the sympathetic cooling regime for $\gamma_p \ll \gamma_p^{\mathrm{eff}}$, where the nanoparticle is cooled by the ion via Coulomb interaction at a rate γ_p^{eff} defined below. In this regime, assuming weak ion-nanoparticle coupling and ion mechanical damping, $|g_j|, \gamma^{\mathrm{dop}} \ll \Omega'_{ji}$ (which is fulfilled for the
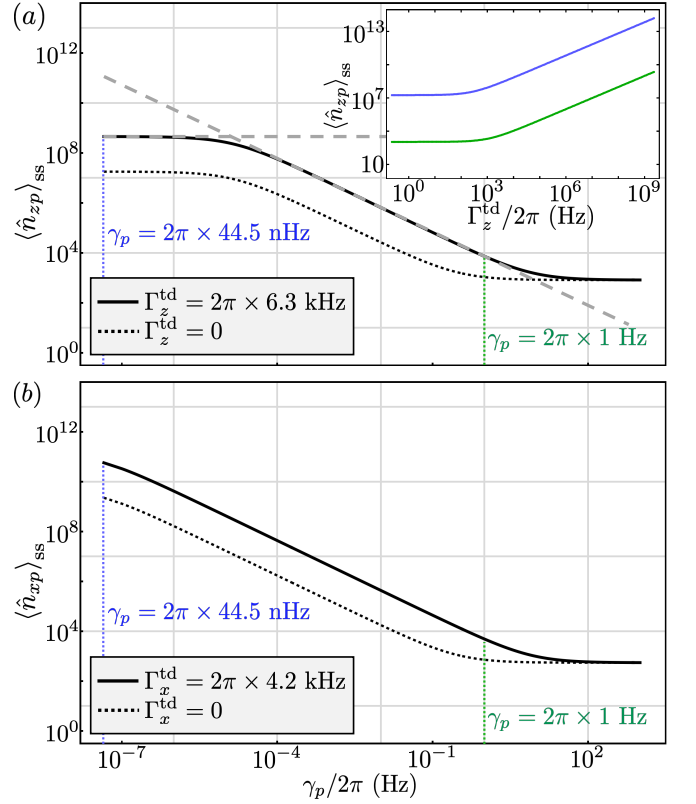

FIG. 3. Steady state phonon number of nanoparticle motion along the $z-$(panel a) and $x-$(panel b) axes versus total damping rate, $\gamma_p = \gamma^{\mathrm{fb}} + \gamma^{\mathrm{gas}}$, for the parameters of Table I. The solid and dotted black curves correspond to the trap-displacement noise values of Ref. [38] and to the case of no trap displacement noise $\Gamma_j^{\mathrm{td}} = 0$, respectively. The horizontal and slanted gray dashed lines show our approximate expressions for the occupation in the sympathetic cooling regime and the feedback cooling regime, Eq. (62) and $\langle \hat{n}_{jp}\rangle_{\mathrm{ss}} \approx \Gamma_{jp}/\gamma^{\mathrm{fb}}$ respectively (see main text for details). The inset in (a) shows the steady state phonon number as a function of the trap-displacement noise in the system, Γ_z^{td}, for $\gamma_p = 2\pi \times 44.5$ nHz (blue) and $\gamma_p = 2\pi \times 1$ Hz (green).

parameters of Table I, see Fig. 2), and neglecting the nanoparticle damping γ_p a simple analytical approximation for the nanoparticle occupation can be derived,

$$\langle \hat{n}_{jp}\rangle_{\mathrm{ss}} \approx \frac{1}{\gamma^{\mathrm{dop}}} \frac{1}{g_j^2} \frac{\left(\Omega'^2_{ji} - \Omega'^2_{jp}\right)^2}{4\Omega'_{ji}\Omega'_{jp}} \Gamma_{jp}. \qquad (61)$$

The above expression, shown by a horizontal dashed line in Fig. 3, highlights the main limitation to the sympathetic cooling, namely the vastly different mechanical frequencies of ion and nanoparticle, $\Omega'^2_{ji} \gg \Omega'^2_{jp}$. From equation (61) we can define the sympathetic cooling rate as $\gamma_p^{\mathrm{eff}} \equiv \langle \hat{n}_{jp}\rangle_{\mathrm{ss}}/\Gamma_{jp}$ which, in the limit $\Omega'^2_{ji} \gg \Omega'^2_{jp}$, reads

$$\gamma_p^{\mathrm{eff}} \approx \gamma^{\mathrm{dop}} \frac{4\Omega'_{jp}}{\Omega'^3_{ji}} g_j^2. \qquad (62)$$

The second regime is the feedback cooling regime $\gamma_p^{\rm eff} \lesssim \gamma^{\rm fb}$, where the damping is dominated by the feedback contribution and the steady-state occupation can be written as $\langle \hat{n}_{jp} \rangle_{\rm ss} \approx \Gamma_{jp}/\gamma^{\rm fb}$. This expression describes an initial linear decrease with $\gamma_p \approx \gamma^{\rm fb}$, followed by a saturation to a constant $\langle \hat{n}_{jp} \rangle_{\rm ss} \to \Gamma_j^{\rm ba}/\gamma^{\rm fb}$ when the measurement backaction rate Eq. (52) becomes dominant over other heating rates. We remark that the onset of this saturation, as well as the minimum reachable occupation, depends strongly on the experimental measurement setup. The results in Fig. 3 correspond to the measurement scheme in Ref. [38], namely $\varepsilon = 2.11$, $\lambda_0 = 780$ nm, and $c_{\rm fb} = 1.57 \times 10^{-6}$ Hz m^2/W, and $\zeta = 7$ [64]. In general, Fig. 3 shows significant sympathetic cooling from room temperature enabled by a single ion, especially along the $z-$axis, where we predict steady-state temperatures $T \approx 23$ K in current experiments and $T \approx 0.92$ K if trap-displacement noise is suppressed. For deeper cooling toward the ground state, however, measurement-based feedback remains the most effective route.

B. Effect of micromotion

When the equilibrium position of the trapped objects is not at the center of the Paul trap, the secular approximation to the ion and nanoparticle Hamiltonians, Eq. (29), can become inaccurate due to micromotion, i.e. due to the terms oscillating at the RF frequencies in Eq. (17) becoming relevant. In this section we quantify the effect of micromotion on sympathetic cooling by solving the master equation Eq. (28), under substitution of the secular Hamiltonian Eq. (29) by the full time-dependent version

$$\hat{H}_\sigma(t) = \frac{\hat{\mathbf{P}}_\sigma^2}{2M_\sigma} + \frac{M_\sigma}{2} \sum_{j=x,y,z} W_{j\sigma}(t) \hat{R}_{j\sigma}^2, \qquad (63)$$

with the function $W_{j\sigma}(t)$ given in Eq. (20). We linearise the Coulomb interaction around the static equilibrium positions, i.e. around the same equilibrium positions $\boldsymbol{D}_i$ and $\boldsymbol{D}_p$ determined only by the secular Hamiltonian and derived in Sec. III A. The linearised Hamiltonian around these static equilibrium positions reads

$$\hat{H}_{\rm tot}(t) = \frac{1}{2}\hat{\boldsymbol{P}}^T \bar{M} \hat{\boldsymbol{P}} + \frac{1}{2}\hat{\boldsymbol{X}}^T \bar{V}_m(t)\hat{\boldsymbol{X}} + \mathbf{F}(t)\hat{\boldsymbol{X}}, \quad (64)$$

where the position and momenta vectors $\hat{\boldsymbol{X}}$ and $\hat{\boldsymbol{P}}$ are defined in Eqs. (35-36), the matrix $\bar{M}$ is defined in Eq. (37), and the new generalised potential matrix takes a similar form as Eq. (38) but with time-dependent frequencies,

$$\bar{V}_m(t) \equiv \begin{bmatrix} -\bar{N}_{\rm coul} & \bar{N}_{\rm coul} \\ \bar{N}_{\rm coul} & -\bar{N}_{\rm coul} \end{bmatrix} + \begin{bmatrix} \bar{V}_{di,m}(t) & \mathbb{0}_{3\times3} \\ \mathbb{0}_{3\times3} & \bar{V}_{dp,m}(t) \end{bmatrix}, \quad (65)$$

with $\bar{V}_{di,m}(t) \equiv M_i {\rm diag}[W_{xi}^2(t), W_{yi}^2(t), W_{zi}^2(t)]$ and $\bar{V}_{dp,m}(t) \equiv M_p {\rm diag}[W_{xp}^2(t), W_{yp}^2(t), W_{zp}^2(t)]$. The Hamiltonian Eq. (64) also contains a time-dependent force

describing the driving of the mean oscillator position due to the RF fields. This vector can be written as $\mathbf{F}(t) = [\mathbf{F}_i(t), \mathbf{F}_p(t)]^T$ with

$$\mathbf{F}_\sigma(t) = M_\sigma \begin{bmatrix} (W_{x\sigma}(t) - \Omega_{x\sigma}^2)d_{x\sigma} \\ (W_{y\sigma}(t) - \Omega_{y\sigma}^2)d_{y\sigma} \\ (W_{z\sigma}(t) - \Omega_{z\sigma}^2)d_{z\sigma} \end{bmatrix}. \qquad (66)$$

The Hamiltonian Eq. (64) is an accurate description of the system provided that each trapped particle remains close to its static equilibrium position even in the presence of micromotion, i.e., $\langle \delta \hat{R}_{j\sigma} \delta \hat{R}_{j'\sigma'} \rangle(t) \ll D^2$. We assume that the dissipators $\mathcal{D}_p(\hat{\rho})$ and $\mathcal{D}_i(\hat{\rho})$ in the master equation Eq. (28) are unaffected by micromotion, but, since the ladder operators $\hat{b}_{j\sigma}$ are not well defined for time-dependent Hamiltonians, we write these dissipators in terms of position and momentum operators $\delta \hat{R}_{j\sigma}$ and $\hat{P}_{j\sigma}$ using the identity $2\hat{b}_{j\sigma} = (\delta \hat{R}_{j\sigma}/R_{j\sigma}^{\rm zpf}) + i(\hat{P}_{j\sigma}/P_{j\sigma}^{\rm zpf})$.

Using the master equation including micromotion we can derive the following equations of motion,

$$\frac{\rm d}{{\rm d}t}\langle \hat{\mathbf{v}} \rangle = \bar{A}_m(t)\langle \hat{\mathbf{v}} \rangle - \begin{bmatrix} \mathbb{0}_{6\times1} \\ \mathbf{F}(t) \end{bmatrix}, \qquad (67)$$

and

$$\frac{\rm d}{{\rm d}t}\bar{\Sigma}_{\rm c} = \bar{A}_m(t)\bar{\Sigma}_{\rm c} + \bar{\Sigma}_{\rm c}\bar{A}_m^T(t) + \bar{C}_m, \qquad (68)$$

where we define the $12-$dimensional quadrature vector $\hat{\mathbf{v}} \equiv [\hat{\mathbf{X}}, \hat{\mathbf{P}}]^T$ and the 12×12 covariance matrix of the quadratures $(\bar{\Sigma}_{\rm c})_{kl} \equiv \langle \hat{v}_k \hat{v}_l + \hat{v}_l \hat{v}_k \rangle/2 - \langle \hat{v}_k \rangle \langle \hat{v}_l \rangle$, and where

$$\bar{A}(t) \equiv \begin{bmatrix} -\bar{\gamma}/2 & \bar{M} \\ -\bar{V}_m(t) & -\bar{\gamma}/2 \end{bmatrix}, \qquad (69)$$

with

$$\bar{\gamma} \equiv \begin{bmatrix} \gamma^{\rm dop}\mathbb{1}_{3\times3} & \mathbb{0}_{3\times3} \\ \mathbb{0}_{3\times3} & (\gamma^{\rm fb} + \gamma^{\rm gas})\mathbb{1}_{3\times3} \end{bmatrix}. \qquad (70)$$

The inhomogeneous matrix term in Eq. (68) is given by

$$\bar{C} = \begin{bmatrix} \bar{C}_{rr} & \mathbb{0}_{6\times6} \\ \mathbb{0}_{6\times6} & \bar{C}_{pp} \end{bmatrix}, \qquad (71)$$

where the diagonal blocks are given by

$$\begin{aligned}
\bar{C}_{rr} = {\rm diag}\Big[&(R_{xi}^{\rm zpf})^2\gamma^{\rm dop}, (R_{yi}^{\rm zpf})^2\gamma^{\rm dop}, (R_{zi}^{\rm zpf})^2\gamma^{\rm dop}, \\
&(R_{xp}^{\rm zpf})^2\gamma^{\rm gas}, (R_{yp}^{\rm zpf})^2\gamma^{\rm gas}, (R_{zp}^{\rm zpf})^2\gamma^{\rm gas}\Big] + \\
+2{\rm diag}\Big[&(R_{xi}^{\rm zpf})^2\Gamma_x^{\rm dop}, (R_{yi}^{\rm zpf})^2\Gamma_y^{\rm dop}, (R_{zi}^{\rm zpf})^2\Gamma_z^{\rm dop}, \\
&(R_{xp}^{\rm zpf})^2\Gamma_x^{\rm gas}, (R_{yp}^{\rm zpf})^2\Gamma_y^{\rm gas}, (R_{zp}^{\rm zpf})^2\Gamma_z^{\rm gas}\Big],
\end{aligned}$$
$$(72)$$

and a similar expression for $\bar{C}_{pp}$ under the substitutions $R_{j\sigma}^{\rm zpf} \to P_{j\sigma}^{\rm zpf}$ and $\Gamma_j^{\rm gas} \to 2\Gamma_{jp} - \Gamma_j^{\rm gas}$.
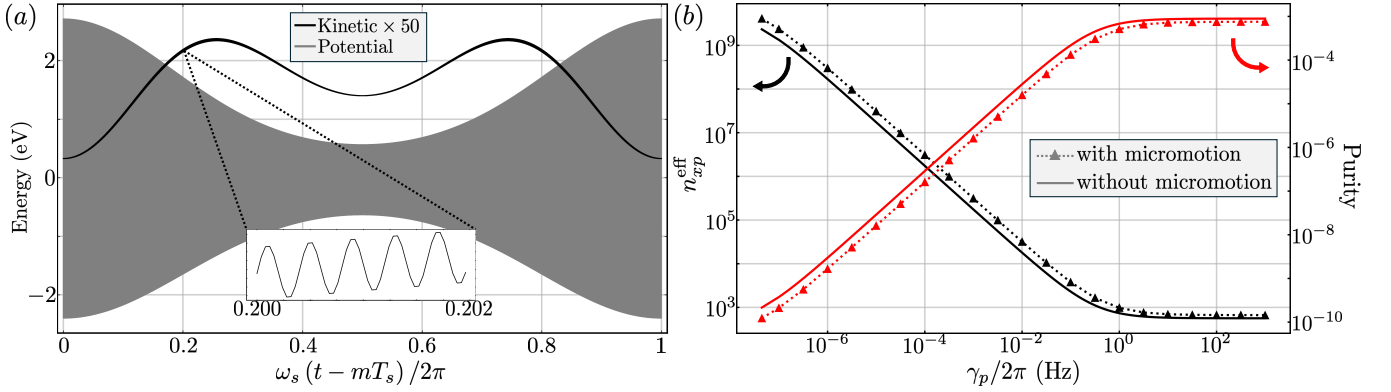
FIG. 4. (a) Potential and kinetic energy of nanoparticle motion along the $x-$axis as a function of time in the long-time limit. The kinetic energy is multiplied by a factor 50 for visibility. The inset shows the fast oscillations of the micromotion at frequency ω_f. (b) Time-averaged purity (Eq. (76)) and effective occupation (Eq. (77)) of the nanoparticle motion along the $x-$axis in the long-time limit as a function of nanoparticle damping $\gamma_p = \gamma^{\mathrm{gas}} + \gamma^{\mathrm{fb}}$. Triangles and solid lines indicate the values with and without micromotion. Parameters are taken from Table I.

By vectorising the covariance matrix we can cast both dynamical Eqs. (67-68) as a Floquet linear system of differential equations of the form $\mathrm{d}\mathbf{f}/\mathrm{d}t = \bar{B}(t)\mathbf{f} + \boldsymbol{w}(t)$ where $\bar{B}(t)$ is, assuming integer l, a periodic matrix with period $T_s = 2\pi/\omega_s$. We compute its solution at long times using Floquet theory [65, 66]. Specifically, the solution at times $mT_s + t$ with $t < T_s$, m integer, and $m \to \infty$, is also a periodic function with period T_s given by

$$\mathbf{f}(mT_s + t) = \bar{X}(t)\Big[\big(\mathbb{1} - \bar{X}(T_s)\big)^{-1} \bar{X}(T_s)\boldsymbol{\Lambda}(T_s) + \boldsymbol{\Lambda}(t)\Big], \quad (73)$$

with

$$\boldsymbol{\Lambda}(t) \equiv \int_0^t \bar{X}(\tau)^{-1}\boldsymbol{w}(\tau)\mathrm{d}\tau. \quad (74)$$

Here $\bar{X}(t)$ is the fundamental matrix solution of the homogeneous system of equations, namely the solution of $\mathrm{d}\bar{X}(t)/\mathrm{d}t = \bar{B}(t)\bar{X}(t)$ with $\bar{X}(0) = \mathbb{1}$. The above expressions reduce the solution of the system of equations to the computation of $\bar{X}(t)$ across one time period only. The solution Eq. (73) is dynamically stable provided that the eigenvalues of the matrix $\bar{X}(T_s)$, denoted by λ_k, lie within the unit circle in the complex plane, i.e.,

$$\max_k \left(|\lambda_k|\right) \leq 1. \quad (75)$$

This is the Floquet stability criterion employed in Secs. III A 1 and V B.

Let us focus on the specific case study considered in this work, where the equilibrium positions of ion and nanoparticle lie along the $z-$axis (i.e. $d_{x\sigma} = d_{y\sigma} = 0$), and the endcaps along z are subject only to a DC potential, i.e. $W_{z\sigma}(t) = \Omega_{z\sigma}^2$. In this case $\mathbf{F}(t) = 0$ and, in analogy with the previous section, the dynamics also

decouples into three subsets of two coupled harmonic oscillators, each corresponding to ion and nanoparticle motion along one cartesian axis. In optimized traps (see Table I) the motion along z is only governed by the DC potential and thus the whole dynamics remains time-independent. In other words, only the motional degrees of freedom along the $x-$ and $y-$axes are affected by micromotion. Since the dynamics along these axes are qualitatively the same, hereafter we focus on the motion along the x direction. We compute the Floquet solution Eq. (73) using the built-in Dormand-Price solver in Python, and show the obtained kinetic and potential energies of the nanoparticle motion in Fig. 4(a). The highly oscillatory behavior is due to the dual-frequency nature of the trap, whose two periods T_s and $T_f \equiv 2\pi/\omega_f \ll T_s$ are inherited by the Floquet solutions. Accurately recovering this fine structure requires a fine time resolution (see inset). Using the Floquet solution, we compute the motional purity of the nanoparticle averaged over one period,

$$\mu_x \equiv \frac{1}{T_s} \int_0^{T_s} \mathrm{d}t \frac{\hbar}{2\sqrt{\det\big(\bar{\Sigma}_{xp}(t)\big)}}, \quad (76)$$

where $\bar{\Sigma}_{jp}$ is the nanoparticle covariance matrix, with $(\bar{\Sigma}_{jp})_{11} = \langle\delta\hat{R}_{jp}^2\rangle - \langle\delta\hat{R}_{jp}\rangle^2$, $(\bar{\Sigma}_{jp})_{22} = \langle\hat{P}_{jp}^2\rangle - \langle\hat{P}_{jp}\rangle^2$, and $(\bar{\Sigma}_{jp})_{12} = (\bar{\Sigma}_{jp})_{21} = \langle\{\delta\hat{R}_{jp}, \hat{P}_{jp}\}\rangle/2 - \langle\delta\hat{R}_{jp}\rangle\langle\hat{P}_{jp}\rangle$. The above expression for the purity is valid for Gaussian states, which always remain Gaussian under quadratic time evolution [67]. From this average purity we define an effective occupation number through the identity [68]

$$n_{xp}^{\mathrm{eff}} \equiv \frac{1}{2}\left(\frac{1}{\mu_x} - 1\right). \quad (77)$$

In the absence of micromotion the above effective occupation becomes the true occupation defined in Sec. IV. Both the average purity and the effective occupation are

displayed in Fig. 4(b) as a function of the nanoparticle damping rate, γ_p, for the same parameters as Fig. 3. Micromotion has a relevant effect on the cooling, increasing the effective occupation by a factor ~ 1.8. These results confirm that the most favorable degree of freedom for quantum levitodynamics is the motion along the $z-$axis which remains unaffected by micromotion.

V. SYMPATHETIC COOLING WITH MULTIPLE IONS

State-of-the-art electrical traps are capable of co-trapping more than one ion along with the nanoparticle [38]. Since all the ions can be individually Doppler-cooled, each can act as an additional energy sink, thus enhancing the performance of sympathetic cooling. In this section, we quantify the scaling of sympathetic cooling with the number of ions. First, we summarize how to generalise our theory to N ions for arbitrary trap parameters in Sec. V A. Then, in Sec. V B, we show the cooling performance of the $N-$ion ensemble for the specific parameters of Table I.

A. Hamiltonian and master equation

To analyze the coupled dynamics of a nanoparticle and $N > 1$ identical ions we generalise the approach employed in Sec. III. We focus on the secular dynamics since, as we will see below, for the parameters considered in this work the micromotion does not affect the motional cooling of the nanoparticle along the $z-$axis. As a first step, we generalise the Coulomb interaction Eq. (30) to multiple ions as

$$V_{ip} = \frac{Q_i}{4\pi\varepsilon_0}\left[\sum_{k=1}^{N}\frac{Q_p}{|\boldsymbol{R}_{i,k} - \boldsymbol{R}_p|} + \sum_{\substack{k=1 \\ l>k}}^{N}\frac{Q_i}{|\boldsymbol{R}_{i,k} - \boldsymbol{R}_{i,l}|}\right].$$
(78)

Note that this expression also includes the all-to-all interactions between the ions. The equilibrium positions of all the objects in the trap, $\{\boldsymbol{D}_{i,1}, ..., \boldsymbol{D}_{i,N}, \boldsymbol{D}_p\}$, are given by the same zero-force condition Eq. (31), which in this case becomes a system of $3N + 3$ nonlinear equations,

$$\left(M_p\Omega_{jp}^2 R_{jp} + \frac{\partial}{\partial R_{jp}}V_{ip}\right)_{\boldsymbol{R}_{i,j}=\boldsymbol{D}_{i,j},\boldsymbol{R}_p=\boldsymbol{D}_p} = 0, \quad (79)$$

$$\left(M_i\Omega_{ji}^2 R_{ji,k} + \frac{\partial}{\partial R_{ji,k}}V_{ip}\right)_{\boldsymbol{R}_{i,j}=\boldsymbol{D}_{i,j},\boldsymbol{R}_p=\boldsymbol{D}_p} = 0, \quad (80)$$

for $j = x, y, z$ and $k = 1, ..., N$. We define displacements from the equilibrium positions as in Eq. (33), namely $\hat{\boldsymbol{R}}_p = \boldsymbol{D}_p + \delta\hat{\boldsymbol{R}}_p$ with $\delta\hat{\boldsymbol{R}}_p = [\delta\hat{R}_{xp}, \delta\hat{R}_{yp}, \delta\hat{R}_{zp}]^T$, and $\hat{\boldsymbol{R}}_{ji,k} = \boldsymbol{D}_{i,k} + \delta\hat{\boldsymbol{R}}_{ji,k}$ with $\delta\hat{\boldsymbol{R}}_{i,k} = [\delta\hat{R}_{xi,k}, \delta\hat{R}_{yi,k}, \delta\hat{R}_{zi,k}]^T$, and linearize the Coulomb interaction Eq. (78) around such equilibrium configuration by expanding it to second order in the variables $\delta\hat{R}_{jp}/|\boldsymbol{D}_p|$ and $\delta\hat{R}_{ji,k}/|\boldsymbol{D}_{i,k}|$. The total linearised Hamiltonian can be written as

$$\hat{H}_{\text{tot}} \equiv \hat{H}_p + \sum_{k=1}^{N}\hat{H}_{i,k} + \hat{V}_{ip} =$$

$$= \frac{1}{2}\hat{\boldsymbol{P}}^T\bar{M}_N\hat{\boldsymbol{P}} + \frac{1}{2}\hat{\boldsymbol{X}}^T\bar{V}_N\hat{\boldsymbol{X}}, \quad (81)$$

where the individual Hamiltonians of the nanoparticle, $\hat{H}_p$, and of each ion, $\hat{H}_{i,k}$, are given by Eq. (29), and where the position and momentum operator vectors are generalised as $\hat{\boldsymbol{X}} = [\delta\hat{\boldsymbol{R}}_{i,1}, \delta\hat{\boldsymbol{R}}_{i,2}, ..., \delta\hat{\boldsymbol{R}}_{i,N}, \delta\hat{\boldsymbol{R}}_p]^T$ and $\hat{\boldsymbol{P}} = [\hat{\boldsymbol{P}}_{i,1}, \hat{\boldsymbol{P}}_{i,2}, ..., \hat{\boldsymbol{P}}_{i,N}, \hat{\boldsymbol{P}}_p]^T$. The inverse mass matrix and generalised potential matrix, $\bar{M}_N$ and $\bar{V}_N$, have dimensions $(3N + 3) \times (3N + 3)$ and read

$$\bar{M}_N \equiv \left[\begin{array}{c|c} M_i^{-1}\mathbb{1}_{3N\times3N} & \mathbb{0}_{3N\times3} \\ \hline \mathbb{0}_{N\times3N} & M_p^{-1}\mathbb{1}_{3\times3} \end{array}\right], \quad (82)$$

and

$$\bar{V}_N \equiv \begin{bmatrix} -\bar{N}_1 - \bar{N}_{1p} + \bar{V}_{di} & \bar{N}_{12} & \bar{N}_{13} & \cdots & \bar{N}_{1p} \\ \bar{N}_{21} & -\bar{N}_2 - \bar{N}_{2p} + \bar{V}_{di} & \bar{N}_{23} & \cdots & \bar{N}_{2p} \\ \bar{N}_{31} & \bar{N}_{32} & -\bar{N}_3 - \bar{N}_{3p} + \bar{V}_{di} & \cdots & \bar{N}_{3p} \\ \vdots & \vdots & \vdots & \ddots & \vdots \\ \bar{N}_{p1} & \bar{N}_{p2} & \bar{N}_{p3} & \cdots & -\sum_{k=1}^{N}\bar{N}_{kp} + \bar{V}_{dp} \end{bmatrix}. \quad (83)$$

Here we have defined the generalised Coulomb matrix (see Eq. (39))

$$\bar{N}_{kl} \equiv \frac{Q_i^2}{4\pi\varepsilon_0|\boldsymbol{D}_{i,k} - \boldsymbol{D}_{i,l}|^3} \times$$

$$\times \left[\mathbb{1}_{3\times3} - 3\frac{(\boldsymbol{D}_{i,k} - \boldsymbol{D}_{i,l})\otimes(\boldsymbol{D}_{i,k} - \boldsymbol{D}_{i,l})}{|\boldsymbol{D}_{i,k} - \boldsymbol{D}_{i,l}|^2}\right], \quad (84)$$

with $k, l = 1, 2, ..., N$, and with $\bar{N}_k = \sum_{l=1, l\neq k}^{N}\bar{N}_{kl}$. The matrices $\bar{N}_{kp} = \bar{N}_{pk}$ have an analogous expression under the substitutions $Q_i^2 \to Q_iQ_p$ and $\boldsymbol{D}_{i,l} \to \boldsymbol{D}_p$.

The Hamiltonian in the form Eq. (81) can be introduced into the secular master equation Eq. (28), which

for the $N-$ion case reads

$$\dot{\hat{\rho}} = -\frac{i}{\hbar}\left[\hat{H}_{\text{tot}}, \hat{\rho}\right] + \mathcal{D}_p\left(\hat{\rho}\right) + \sum_{k=1}^{N}\mathcal{D}_{i,k}\left(\hat{\rho}\right). \quad (85)$$

Here $\hat{\rho}$ is the density matrix of the motional degrees of freedom of the N ions and the nanoparticle, and $\mathcal{D}_p$ and each of the ion dissipators $\mathcal{D}_{i,k}$ are given by Eqs. (47) and Eq. (54) respectively. From the above master equation the steady-state occupation of each degree of freedom can be extracted as detailed in Sec. IV.

B. Results

Let us focus on the results obtained for the parameters of Table I. First, we obtain the stable equilibrium positions by solving the nonlinear system of Eqs. (79-80) for each value of N using SciPy's root-finding function. We perform a two-step search for multiple equilibrium positions: first, for $N \leq 8$, we run the solver $5000 + N!$ times, each with different seed values for the $3N + 3$ spatial coordinates of all the objects. At each run, the seed values are drawn randomly within a cubic box of size 200 μm $\times$ 200 μm $\times$ 200 μm centered at the origin. From each of the found equilibrium configurations, we retain only those which fulfill *both* the dynamical and the Floquet stability criteria, defined respectively in Secs. III A 1 and IV B (See Eqs. (41) and (75) respectively). Similarly to the $N = 1$ case, all the found stable configurations correspond to the equilibrium positions of all the objects – nanoparticle and all N ions – lying along the $z-$axis, as shown by the examples in Fig. 5(a). We ascribe this to the fact that this configuration minimises the negative Coulomb-induced shift in the mechanical frequencies along the $z-$axis. More specifically, as shown by Eq. (40), due to the Coulomb interaction the trap frequencies of any two objects are always reduced in the directions orthogonal to the line connecting them. If this shift is large enough the mechanical frequencies can approach zero or even become imaginary, corresponding to an unstable potential. When all objects lie along the $z-$axis only the radial trapping frequencies $\{\Omega_{xp}, \Omega_{yp}, \Omega_{xi,k}, \Omega_{yi,k}\}$ decrease, whereas for any other configuration the longitudinal frequencies Ω_{zp} and $\Omega_{zi,k}$ also do. Since $\Omega_{zp} < \Omega_{xp}, \Omega_{yp}$ and $\Omega_{zi,k} < \Omega_{xi,k}, \Omega_{yi,k}$ (see Table I), the Coulomb-induced shift has a stronger de-stabilising effect in the latter case as it reduces frequencies that are already small. Hence, configurations where all objects lie along the $z-$axis tend to be more stable.

Using the above insight, for the second step of our search ($N > 8$) we search only for equilibrium configurations where all the objects lie exactly along the $z-$axis. We set the x, y coordinates of each object to zero and run the same search algorithm $10^4 N$ times. At each run the initial $z-$coordinates for each object are drawn randomly within the segment $|z| < 100$ μm. We retain only

the solutions for which the full $(3N+3) \times (3N+3)$ Hamiltonian is dynamically and Floquet-stable [69]. No stable solutions were found for $13 \leq N \leq 20$, suggesting that $N = 12$ is the maximum amount of ions that can be co-trapped along a single axis for the chosen parameter values. However, we remark that this is not a fundamental limitation but rather a constraint imposed by the choice of parameters in Table I. For instance, increasing the trap stiffness in the radial directions could enable trapping more ions in this configuration. We do not explore such improvements in this work as $N \leq 12$ is sufficient for the purposes of this section, namely to quantify the scaling of sympathetic cooling performance with N.

Since the equilibrium positions lie on the $z-$axis, the motional degrees of freedom along each axis decouple. We thus focus hereafter only on the dynamics of each object along the $z-$axis, which is governed by the $(N + 1) \times (N + 1)$ Hamiltonian (see Eq. (81))

$$\hat{H}_{\text{tot}}^{(z)} = \hat{H}_p^{(z)} + \sum_{k=1}^{N}\hat{H}_{i,k}^{(z)} + \sum_{k=1}^{N}\delta\hat{R}_{zi,k}$$
$$\times \left(\left(\bar{N}_{kp}\right)_{33}\delta\hat{R}_{zp} + \sum_{l>k}\left(\bar{N}_{kl}\right)_{33}\delta\hat{R}_{zi,l}\right), \quad (86)$$

with

$$\hat{H}_p^{(z)} = \frac{\hat{P}_{zp}^2}{2M_p} + \frac{M_p}{2}\Omega_{zp}^{'2}\delta\hat{R}_{zp}^2, \quad (87)$$

and a similar expression for the individual ion Hamiltonians $\hat{H}_{i,k}^{(z)}$ under the substitution $\{M_p, \Omega_{zp}', \hat{P}_{zp}, \delta\hat{R}_{zp}\} \rightarrow \{M_i, \Omega_{zi,k}', \hat{P}_{zi,k}, \delta\hat{R}_{zi,k}\}$. The dissipative dynamics within this subspace is given by the terms within $\mathcal{D}_p(\hat{\rho})$ and $\mathcal{D}_{i,k}(\hat{\rho})$ containing operators corresponding to motion along z.

Using the Hamiltonian Eq. (86) and the equilibrium positions obtained above, we numerically compute the steady-state occupation of the nanoparticle motion along the $z-$axis, $\langle\hat{n}_{zp}\rangle_{\text{ss}}$. For each value of N multiple stable equilibrium configurations exist, but they result in very similar values for $\langle\hat{n}_{zp}\rangle_{\text{ss}}$ with deviations of $\sim 0.01\%$. We choose the best equilibrium configurations, namely those for which the steady-state occupation $\langle\hat{n}_{zp}\rangle_{\text{ss}}$ is lowest, and show the corresponding occupation as a function of the number of ions in Fig. 5(b) (black curve) in the absence of trap-displacement noise, $\Gamma_z^{\text{td}} = 0$. The nanoparticle occupation decreases as $\sim 1/N$, reaching an occupation $\langle\hat{n}_{zp}\rangle_{\text{ss}} = 1.5 \times 10^6$ for $N = 12$ corresponding to a motional temperature of 77 mK, which is a factor $\simeq 12.2$ lower than the single-ion case in Fig. 3. The green line in Fig. 5(b) shows the occupation predicted by an independent ion model, namely $\langle\hat{n}_{zp}\rangle_{\text{ss}} = \Gamma_z^{\text{gas}}/\sum_{k=1}^{N}\gamma_{p,k}^{\text{eff}}$, where the cooling rate $\gamma_{p,k}^{\text{eff}}$ for each ion is defined by Eq. (62) under the substitution $g_z \rightarrow g_{z,k}$ and $\Omega_{zi}' \rightarrow \Omega_{zi,k}'$. Note that for this expression, we neglect the Coulomb interaction between different ion motional degrees of freedom,
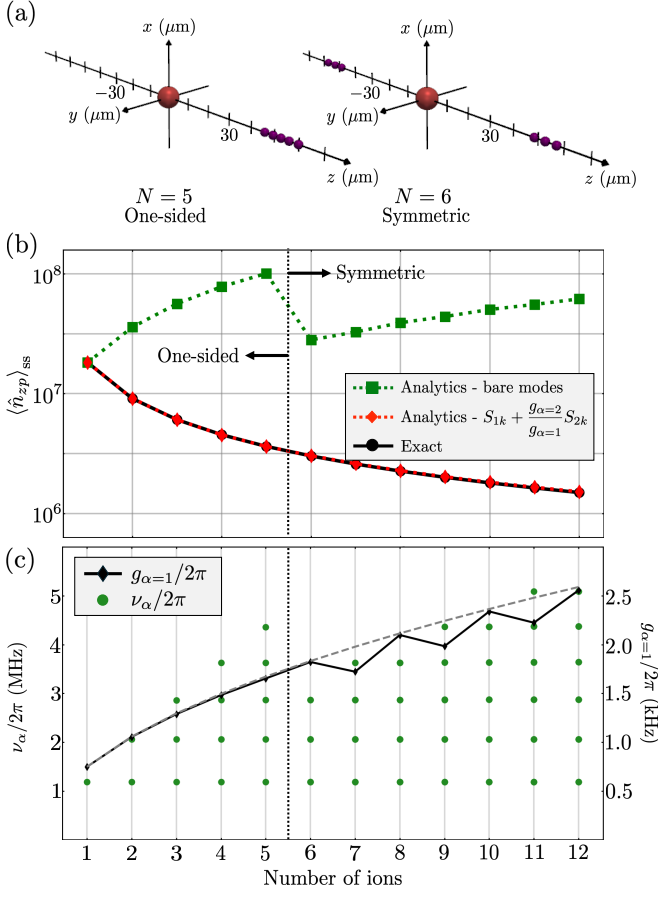
FIG. 5. (a) Optimal ion and nanoparticle equilibrium positions for sympathetic cooling, for $N = 5$ and $N = 6$ ions, respectively. (b) Steady state motional occupation of the nanoparticle along the $z-$axis, $\langle \hat{n}_{zp} \rangle_{\text{ss}}$, versus ion number N, for the best-performing equilibrium configuration for each N. Parameters are taken from Table I, with trap-displacement noise $\Gamma_z^{\text{td}} = 0$. The exact solution (black) is compared to an independent-ion model (green, see text for details) and to a model where only the center-of-mass mode of the chain couples to the nanoparticle motion (red, Eq. (92)). (c) Normal mode frequencies of the $N-$ion system (green circles) and coupling rate between nanoparticle and normal mode $\alpha = 1$ (black). The dashed gray curves show a $\sqrt{N}$ scaling. The vertical dotted lines in panels (b-c) mark the transition between one-sided and symmetric equilibrium configurations.

but include the associated Coulomb shift in the ion trap frequencies $\Omega'_{zi,k}$. This shift strongly stiffens the ion trapping potentials as N increases, increasing the detuning between ion and nanoparticle motional frequencies $\Omega'_{zi,k} - \Omega'_{zp}$ and thus decreasing the cooling performance. The sharp decrease at $N = 6$ is caused by a qualitative change in the best equilibrium configurations, which for $N \leq 5$ correspond to all ions lying on one side of the nanoparticle and for $N \geq 6$ to ions evenly split on both sides (see Fig. 5(a)). In general, the independent-ion approximation clearly fails to capture the behavior of the nanoparticle occupation, indicating that the mo-

tional coupling between the ions plays a crucial role in the sympathetic cooling.

To gain a deeper understanding of the sympathetic cooling process, we perform a symplectic diagonalisation of the ion Hamiltonian to obtain its normal modes. That is, we define a transformation

$$\hat{Q}_\alpha \equiv \sum_{k=1}^{N} \sqrt{M_i} S_{\alpha k} \delta \hat{R}_{zi,k}, \qquad (88)$$

and

$$\hat{\Pi}_\alpha \equiv \sum_{k=1}^{N} \frac{S_{\alpha k} \hat{P}_{zi,k}}{\sqrt{M_i}}, \qquad (89)$$

where the new coordinates obey canonical commutation relations, $\left[\hat{Q}_\alpha, \hat{\Pi}_{\alpha'} \right] = i\hbar \delta_{\alpha \alpha'}$, and where $S_{\alpha k}$ is an orthogonal matrix that diagonalises the ion part of the Hamiltonian Eq. (86) and that is calculated numerically. In terms of these new coordinates, the Hamiltonian Eq. (86) takes the form

$$\hat{H}_{\text{tot}}^{(z)} = \hat{H}_p^{(z)} + \sum_{\alpha=1}^{N} \left(\frac{\hat{\Pi}_\alpha^2}{2} + \frac{1}{2} \nu_\alpha^2 \hat{Q}_\alpha^2 \right) +$$
$$+ \delta \hat{R}_{zp} \sum_{\alpha=1}^{N} \hat{Q}_\alpha \sum_{k=1}^{N} \frac{S_{\alpha k} \left(\bar{N}_{kp} \right)_{33}}{\sqrt{M_i}}. \qquad (90)$$

The coordinates $\hat{Q}_\alpha$ correspond to the normal modes of the $N-$ion ensemble, with the rows of $S_{\alpha k}$ determining the amplitude of motion of ion k in mode α. The above Hamiltonian thus describes a set of independent modes, each coupled to the nanoparticle motional coordinate at a rate

$$g_\alpha \equiv \frac{1}{2} \sqrt{\frac{1}{M_i M_p \Omega'_{zp} \nu_\alpha}} \sum_{k=1}^{N} S_{\alpha k} \left(\bar{N}_{kp} \right)_{33}. \qquad (91)$$

The normal mode frequencies ν_α are shown in Fig. 5(c). They have a very weak dependence on N, as has already been pointed out in the literature [70].

We will first focus on sympathetic cooling for $N \geq 6$. In this case, the lowest frequency $\nu_\alpha \approx 2\pi \times 1.2$ MHz corresponds to a pair of quasi-degenerate modes which we label $\alpha = 1$ and $\alpha = 2$. The mode displacements $S_{\alpha k}$ for these two modes are shown in Fig. 6 for N even (panels a-b) and N odd (panels c-d). For N even the mode $\alpha = 1$ corresponds to the center-of-mass mode where all ions oscillate in phase with approximately equal amplitudes, whereas the $\alpha = 2$ mode corresponds to a breathing mode where the two ion chains oscillate with opposite phases. In contrast, for N odd the asymmetry between the two ion chains manifests in different motional amplitudes for each chain. In this case, the center-of-mass mode is a linear combination of both modes $\alpha = 1$ and $\alpha = 2$ with weights $g_{\alpha=1}$ and $g_{\alpha=2}$. We expect the sympathetic cooling to be dominated by the center-of-mass mode as the

forces exerted by each ion onto the nanoparticle add up constructively at all times. This is confirmed by the red curve in Fig. 5(b) which shows the approximate occupation, $\langle \hat{n}_{zp} \rangle_{\rm ss} \approx \Gamma_z^{\rm gas}/\gamma_p^{\rm eff,N}$, using an effective cooling rate similar to Eq. (62), but including only normal modes that contribute to the center-of-mass mode,

$$\gamma_p^{\rm eff,N} = \gamma_{p,\alpha=1}^{\rm eff} + \gamma_{p,\alpha=2}^{\rm eff}\delta_{N,\rm odd}$$
$$\approx \gamma^{\rm dop}\frac{4\Omega_{zp}'}{\nu_1^3} \times \begin{cases} g_{\alpha=1}^2 & (N \text{ even}) \\ g_{\alpha=1}^2 + g_{\alpha=2}^2 & (N \text{ odd}) \end{cases} \quad (92)$$

In the last step we have used $\nu_{\alpha=1} \approx \nu_{\alpha=2}$ and approximated the cooling rates of both normal modes as the single-ion cooling rate $\gamma^{\rm dop}$, an approximation that is valid for any mode α fulfilling $|\nu_\alpha - \Omega_{zi}'| \ll \sqrt{\nu_\alpha \Omega_{zi}'}$. For $N \leq 5$ a similar argument can be made, the only difference being that the lowest normal mode frequency $\nu_\alpha \approx 2\pi \times 1.2$ MHz corresponds to the non-degenerate center-of-mass mode of the ion chain for both N even and N odd. As a consequence the coupling between nanoparticle and other normal modes is also small for both N even and N odd, specifically $g_{\alpha=2}^2 \ll g_{\alpha=1}^2$. Because of this, the expression for the effective cooling rate Eq. (92) remains valid for $N \leq 5$.

Equation (92) provides a useful resource to estimate the cooling rate expected in general setups, as well as its scaling with N. Specifically, the only factors in the cooling rate Eq. (92) that significantly depend on the ion number N are the normal mode coupling rates g_α, which display the $\sqrt{N}$ scaling characteristic of homogeneous coupling to multiple degrees of freedom (see e.g. the coupling $g_{\alpha=1}$ displayed in Fig. 5(c)). This results in a scaling $\gamma_p^{\rm eff,N} \sim N$ for the cooling rate and fully explains the scaling $\langle \hat{n}_{zp} \rangle_{\rm ss} \sim 1/N$ for the occupation observed in Fig. 5(b). This scaling suggests that sympathetic cooling is unlikely to enable cooling of the nanoparticle motion to the ground state, as co-trapping $\sim 10^6 - 10^7$ ions is technically challenging. Our results thus highlight the relevance of devising new methods to increase sympathetic cooling efficiency.

VI. CONCLUSION

We have derived a theory to describe the quantum dynamics of a levitated nanoparticle co-trapped with an ion ensemble in a dual-frequency Paul trap. We have used it to quantify the performance of ion-based sympathetic cooling in levitodynamics and to provide analytical estimates of the nanoparticle occupations, which apply to a wide variety of electric trap geometries and parameters. For state-of-the-art experiments, our theory predicts ion-based sympathetic cooling of the nanoparticle motion below 1 K using a single ion, and below 1 mK using the center-of-mass mode of an ensemble of $N = 12$ ions. We have identified the main limitations of this scheme to be high trap-displacement noise rates $\Gamma_j^{\rm td}$ and, most importantly, the vast difference between ion and nanoparticle
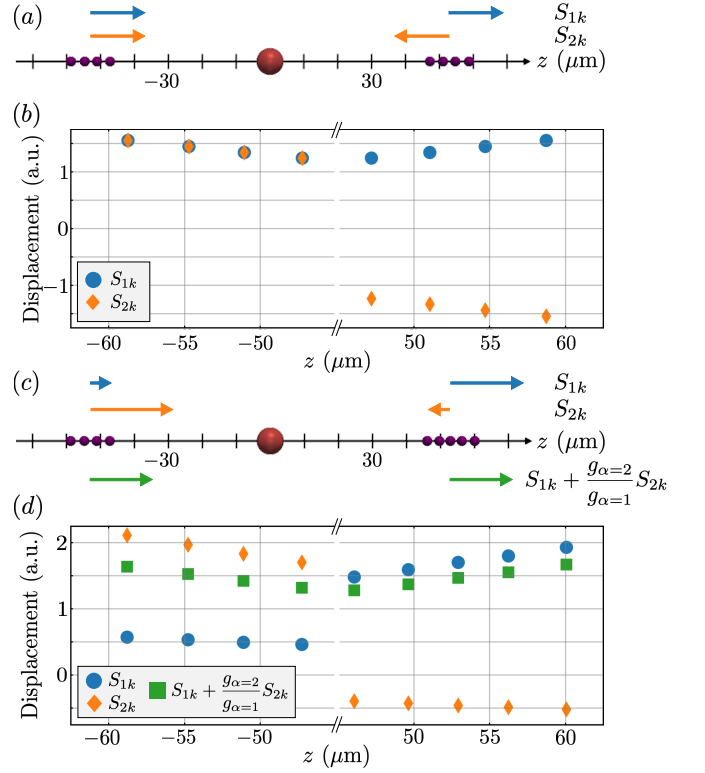

FIG. 6. Ion displacements in the first two normal modes, S_{k1} (blue) and S_{k2} (orange) for $N = 8$ (panels a-b) and $N = 9$ ions (panels c-d). The arrow lengths in (a,c) are proportional to the average ion displacement on each chain. The nanoparticle motion couples predominantly to the center-of-mass mode of the ion ensemble, which for N odd is a linear combination of the $\alpha = 1$ and $\alpha = 2$ modes (green arrows / dots).

mechanical frequencies, Ω_{ji}' and Ω_{jp}'. To obtain insight into these limitations, we can set $\Gamma_j^{\rm td} = 0$ and equal mechanical frequencies, $\Omega_{ji}' = \Omega_{jp}' = 2\pi \times 1$ kHz in our model, while keeping the same values used throughout this work for the remaining parameters. This choice results in a predicted steady-state nanoparticle occupation of ~ 110 phonons using a single ion, in the absence of optical feedback and without optimizing other parameters. Future efforts toward ground-state cooling should thus be aimed not only at reducing unwanted noise, but also at bridging this frequency gap, for instance through coupling both particle and ions to the same optical cavity [42]. A second option is to modulate the distance between ion and nanoparticle, and thus their Coulomb coupling, at a frequency $\Omega_{ji}' - \Omega_{jp}'$ in order to parametrically amplify the sympathetic cooling. This modulation could be achieved in free space, i.e., without the need for cavities, by, e.g., applying an AC voltage to one of the endcap electrodes.

Beyond sympathetic cooling, the theory we have developed has enabled us to provide analytical expressions for all system parameters, including the secular motional frequencies, coupling rates, and equilibrium positions of ion

and nanoparticle. Our work thus provides the theoretical toolbox needed to describe ion-nanoparticle levitodynamics experiments in the quantum regime. Moreover, it opens the door to assess the feasibility of protocols to prepare quantum motional states of electrically levitated nanoparticles without the use of light.

Appendix A: Exact expression for nanoparticle occupation

The nanoparticle occupation obtained from Eq. (57) can be cast as

$$\langle \hat{n}_{jp} \rangle_{\text{ss}} = \frac{32\tilde{g}_j^4 n_1 - k\chi\tilde{\gamma}^{\text{dop}}\tilde{\Gamma}_{jp}n_2 + 4\tilde{g}_j^2\tilde{\gamma}^{\text{dop}}n_3}{\tilde{\gamma}^{\text{dop}}\left(4k\chi - 64\tilde{\gamma}^{\text{dop2}}\tilde{g}_j^2\tilde{\Omega}_{jp}\right)\left(64\gamma_+^2\tilde{g}_j^2\tilde{\Omega}_{jp} + \gamma_\times n_2\right)}, \tag{A1}$$

where tilded variables represent variables normalized to the ion mechanical frequency, e.g. $\tilde{\gamma}^{\text{dop}} \equiv \gamma^{\text{dop}}/\Omega'_{ji}$, and with

$$n_1 \equiv \left(\gamma_\times\gamma_+ h_3 + \tilde{\gamma}^{\text{dop3}}\left(4 + \gamma_+\tilde{\gamma}^{\text{dop2}}\right)\right)\left(\gamma_\times + 2\tilde{\gamma}^{\text{dop}}\tilde{\Gamma}_{jp}\right) - \tilde{A}\left(\gamma_\times^2 h_2 + 8k\tilde{\gamma}^{\text{dop2}}h_{1/2}\right)\tilde{\Omega}_{jp}$$
$$+ 4\tilde{\gamma}^{\text{dop}}\left(h_2^2 - 6\tilde{\gamma}^{\text{dop}}\tilde{\Gamma}_{jp}h_{4/3}\right)\tilde{\Omega}_{jp}^2 - 4\tilde{A}\tilde{\gamma}^{\text{dop2}}h_2\tilde{\Omega}_{jp}^3, \tag{A2}$$

$$n_2 \equiv \left(\gamma_+^2 + 4\left(1 + \tilde{\Omega}_{jp}^2\right)\right)^2 - 64\tilde{\Omega}_{jp}^2, \tag{A3}$$

and

$$n_3 \equiv k\gamma_\times^2\gamma_+\left(4 + \gamma_+^2\right)\tilde{A} - 8k\gamma_\times^2\gamma_+\tilde{\gamma}^{\text{dop}}\tilde{\Omega}_{jp} - 4\left(-4\gamma_\times\gamma_+ h_{-2} + \gamma_\times^2\gamma_+ h_2 + 3\gamma_+\tilde{\gamma}^4 h_{1/3} + 16\tilde{\gamma}^{\text{dop3}} + 8\gamma_+\tilde{\gamma}^{\text{dop4}}\right)\tilde{\Gamma}_{jp}\tilde{\Omega}_{jp}$$
$$+ 8k\gamma_+\tilde{A}\left(2k\tilde{\gamma}^{\text{dop2}} + \gamma_\times h_1\right)\tilde{\Omega}_{jp}^2 - 8\tilde{\gamma}^{\text{dop}}\left(4k\gamma_+\tilde{\gamma}^{\text{dop2}} + 2\left(-4h_3 + 2\gamma_\times h_{3/2} + \tilde{\gamma}^{\text{dop4}}\right)\tilde{\Gamma}_{jp}\right)\tilde{\Omega}_{jp}^3$$
$$+ 16k\gamma_+\tilde{A}\tilde{\gamma}^{\text{dop2}}\tilde{\Omega}_{jp}^4 - 64\tilde{\gamma}^{\text{dop3}}\tilde{\Gamma}_{jp}\tilde{\Omega}_{jp}^5, \tag{A4}$$

and where we have defined $\tilde{A} \equiv \tilde{\gamma}^{\text{dop}} + 2\tilde{\Gamma}_j^{\text{dop}}$, $k \equiv (\tilde{\gamma}^{\text{dop}}/2)^2 + 1$, $\gamma_+ = \tilde{\gamma}_p + \tilde{\gamma}^{\text{dop}}$, $\gamma_\times = \tilde{\gamma}_p\tilde{\gamma}^{\text{dop}}$, $h_\eta \equiv \gamma_\times + \eta\gamma_+^2$, and $\chi \equiv \gamma_\times^2 + 4\tilde{\gamma}^{\text{dop2}}\tilde{\Omega}_{jp}^2$. Here, $\gamma_p \equiv \gamma^{\text{gas}} + \gamma^{\text{fb}}$ is the total damping rate of the nanoparticle.

[1] J. Millen, T. S. Monteiro, R. Pettit, and A. N. Vamivakas, Reports on Progress in Physics **83**, 026401 (2020).

[2] C. Gonzalez-Ballestero, M. Aspelmeyer, L. Novotny, R. Quidant, and O. Romero-Isart, Science **374**, eabg3027 (2021).

[3] U. Delić, M. Reisenbauer, K. Dare, D. Grass, V. Vuletić, N. Kiesel, and M. Aspelmeyer, Science **367**, 892 (2020).

[4] F. Tebbenjohanns, M. L. Mattana, M. Rossi, M. Frimmer, and L. Novotny, Nature **595**, 378 (2021).

[5] L. Magrini, P. Rosenzweig, C. Bach, A. Deutschmann-Olek, S. G. Hofer, S. Hong, N. Kiesel, A. Kugi, and M. Aspelmeyer, Nature **595**, 373 (2021).

[6] M. Kamba, R. Shimizu, and K. Aikawa, Opt. Express **30**, 26716 (2022).

[7] A. Ranfagni, K. Børkje, F. Marino, and F. Marin, Phys. Rev. Res. **4**, 033051 (2022).

[8] J. Piotrowski, D. Windey, J. Vijayan, C. Gonzalez-Ballestero, A. de los Ríos Sommer, N. Meyer, R. Quidant, O. Romero-Isart, R. Reimann, and L. Novotny, Nature Physics **19**, 1009 (2023).

[9] L. Dania, O. S. Kremer, J. Piotrowski, D. Candoli, J. Vijayan, O. Romero-Isart, C. Gonzalez-Ballestero, L. Novotny, and M. Frimmer, Nature Physics (2025).

[10] M. Rossi, A. Militaru, N. Carlon Zambon, A. Riera-Campeny, O. Romero-Isart, M. Frimmer, and L. Novotny, Phys. Rev. Lett. **135**, 083601 (2025).

[11] M. Kamba, N. Hara, and K. Aikawa, Science **389**, 1225 (2025).

[12] V. Jain, J. Gieseler, C. Moritz, C. Dellago, R. Quidant, and L. Novotny, Phys. Rev. Lett. **116**, 243601 (2016).

[13] O. Romero-Isart, A. C. Pflanzer, F. Blaser, R. Kaltenbaek, N. Kiesel, M. Aspelmeyer, and J. I.

Cirac, Phys. Rev. Lett. **107**, 020405 (2011).

[14] O. Romero-Isart, Phys. Rev. A **84**, 052121 (2011).

[15] J. Bateman, S. Nimmrichter, K. Hornberger, and H. Ulbricht, Nature Communications **5**, 4788 (2014).

[16] L. Neumeier, M. A. Ciampini, O. Romero-Isart, M. Aspelmeyer, and N. Kiesel, Proceedings of the National Academy of Sciences **121**, e2306953121 (2024).

[17] M. Roda-Llordes, A. Riera-Campeny, D. Candoli, P. T. Grochowski, and O. Romero-Isart, Phys. Rev. Lett. **132**, 023601 (2024).

[18] S. Casulleras, P. T. Grochowski, and O. Romero-Isart, Phys. Rev. A **110**, 033511 (2024).

[19] O. Romero-Isart, L. Clemente, C. Navau, A. Sanchez, and J. I. Cirac, Phys. Rev. Lett. **109**, 147205 (2012).

[20] J. Millen, P. Z. G. Fonseca, T. Mavrogordatos, T. S. Monteiro, and P. F. Barker, Phys. Rev. Lett. **114**, 123602 (2015).

[21] P. Z. G. Fonseca, E. B. Aranas, J. Millen, T. S. Monteiro, and P. F. Barker, Phys. Rev. Lett. **117**, 173602 (2016).

[22] B. R. Slezak, C. W. Lewandowski, J.-F. Hsu, and B. D'Urso, New Journal of Physics **20**, 063028 (2018).

[23] G. P. Conangla, R. A. Rica, and R. Quidant, Nano Letters **20**, 6018 (2020).

[24] D. S. Bykov, M. Meusburger, L. Dania, and T. E. Northup, Review of scientific instruments **93** (2022).

[25] M. Gutierrez Latorre, G. Higgins, A. Paradkar, T. Bauch, and W. Wieczorek, Phys. Rev. Appl. **19**, 054047 (2023).

[26] J. Hofer, R. Gross, G. Higgins, H. Huebl, O. F. Kieler, R. Kleiner, D. Koelle, P. Schmidt, J. A. Slater, M. Trupke, K. Uhl, T. Weimann, W. Wieczorek, and M. Aspelmeyer, Phys. Rev. Lett. **131**, 043603 (2023).

[27] B. Melo, M. T. Cuairan, G. F. M. Tomassi, N. Meyer, and R. Quidant, Nature Nanotechnology **19**, 1270 (2024).

[28] E. Bonvin, L. Devaud, M. Rossi, A. Militaru, L. Dania, D. S. Bykov, O. Romero-Isart, T. E. Northup, L. Novotny, and M. Frimmer, Phys. Rev. Lett. **132**, 253602 (2024).

[29] E. Bonvin, L. Devaud, M. Rossi, A. Militaru, L. Dania, D. S. Bykov, M. Teller, T. E. Northup, L. Novotny, and M. Frimmer, Phys. Rev. Res. **6**, 043129 (2024).

[30] J. J. Hansen, S. Minniberger, D. Ilk, P. Asenbaum, G. Higgins, R. G. Povey, P. Schmidt, J. Hofer, R. Claessen, M. Aspelmeyer, and M. Trupke, arXiv preprint (2025).

[31] D. S. Bykov, P. Mestres, L. Dania, L. Schmöger, and T. E. Northup, Applied Physics Letters **115** (2019).

[32] D. Goldwater, B. A. Stickler, L. Martinetz, T. E. Northup, K. Hornberger, and J. Millen, Quantum Science and Technology **4**, 024003 (2019).

[33] L. Dania, D. Bykov, P. Mestres, and T. E. Northup, in *Optical Trapping and Optical Micromanipulation XVI*, Vol. 11083, edited by K. Dholakia and G. C. Spalding, International Society for Optics and Photonics (SPIE, 2019) p. 1108335.

[34] N. P. Bullier, A. Pontin, and P. F. Barker, Journal of Physics D: Applied Physics **53**, 175302 (2020).

[35] L. Martinetz, K. Hornberger, J. Millen, M. S. Kim, and B. A. Stickler, npj Quantum Information **6**, 101 (2020).

[36] L. Dania, D. S. Bykov, M. Knoll, P. Mestres, and T. E. Northup, Phys. Rev. Res. **3**, 013018 (2021).

[37] L. Dania, D. S. Bykov, F. Goschin, M. Teller, A. Kassid, and T. E. Northup, Phys. Rev. Lett. **132**, 133602 (2024).

[38] D. S. Bykov, L. Dania, F. Goschin, and T. E. Northup, Phys. Rev. Lett. **135**, 213602 (2025).

[39] T. Seberson, P. Ju, J. Ahn, J. Bang, T. Li, and F. Robicheaux, J. Opt. Soc. Am. B **37**, 3714 (2020).

[40] T. W. Penny, A. Pontin, and P. F. Barker, Phys. Rev. Res. **5**, 013070 (2023).

[41] D. S. Bykov, L. Dania, F. Goschin, and T. E. Northup, Optica **10**, 438 (2023).

[42] A. C. Pflanzer, O. Romero-Isart, and J. I. Cirac, Phys. Rev. A **88**, 033804 (2013).

[43] M. Toroš, S. Bose, and P. F. Barker, Phys. Rev. Res. **3**, 033218 (2021).

[44] M. Schut and V. Scarani, Proposal for macroscopic delocalisation of a large mass in a rf trap (2025), arXiv:2509.17081 [quant-ph].

[45] H. Dehmelt, Physica Scripta **1995**, 423 (1995).

[46] D. Trypogeorgos and C. J. Foot, Phys. Rev. A **94**, 023609 (2016).

[47] N. Leefer, K. Krimmel, W. Bertsche, D. Budker, J. Fajans, R. Folman, H. Häffner, and F. Schmidt-Kaler, Hyperfine Interactions **238**, 12 (2016).

[48] M. Teller, V. Messerer, K. Schüppert, Y. Zou, D. A. Fioretto, M. Galli, P. C. Holz, J. Reichel, and T. E. Northup, AVS Quantum Science **5**, 012001 (2023).

[49] I. Pogorelov, T. Feldker, C. D. Marciniak, L. Postler, G. Jacob, O. Krieglsteiner, V. Podlesnic, M. Meth, V. Negnevitsky, M. Stadler, B. Höfer, C. Wächter, K. Lakhmanskiy, R. Blatt, P. Schindler, and T. Monz, PRX Quantum **2**, 020343 (2021).

[50] D. Leibfried, R. Blatt, C. Monroe, and D. Wineland, Rev. Mod. Phys. **75**, 281 (2003).

[51] D. J. Berkeland, J. D. Miller, J. C. Bergquist, W. M. Itano, and D. J. Wineland, Journal of Applied Physics **83**, 5025 (1998).

[52] P. Amore and A. Aranda, Physics Letters A **316**, 218 (2003).

[53] V. Saxena and K. Shah, IEEE Transactions on Plasma Science **46**, 474 (2018).

[54] Note that Eq. (8) has two solutions for β^2. Here we choose the solution that recovers the known behavior in the limit of a single-frequency trap, namely Eq. (9).

[55] P. K. Ghosh, *Ion Traps* (Oxford University Press, Oxford, 1995).

[56] V. Lanchares, Monografías Matemáticas García de Galdeano **39**, 155 (2014).

[57] K. Kustura, C. C. Rusconi, and O. Romero-Isart, Phys. Rev. A **99**, 022130 (2019).

[58] L. Diósi, Europhysics Letters **30**, 63 (1995).

[59] C. Gonzalez-Ballestero, P. Maurer, D. Windey, L. Novotny, R. Reimann, and O. Romero-Isart, Phys. Rev. A **100**, 013805 (2019).

[60] T. Li, S. Kheifets, and M. G. Raizen, Nature Physics **7**, 527 (2011).

[61] S. A. Beresnev, V. G. Chernyak, and G. A. Fomyagin, Journal of Fluid Mechanics **219**, 405–421 (1990).

[62] P. Maurer, C. Gonzalez-Ballestero, and O. Romero-Isart, Phys. Rev. A **108**, 033714 (2023).

[63] J. Eschner, G. Morigi, F. Schmidt-Kaler, and R. Blatt, J. Opt. Soc. Am. B **20**, 1003 (2003).

[64] Note that in regards to experiment Ref. [38], this choice of ζ leads to an overestimation of the heating rate, as it assumes a probe beam propagating exactly along the motional axis.

[65] V. A. Iakubovich and V. M. Starzhinskiĭ, *Linear differential equations with periodic coefficients* (Wiley and Israel Program for Scientific Translations, 1975).

[66] J. Slane and S. Tragesser, Nonlinear Dynamics and Systems Theory **11**, 183 (2011).

[67] T. Barthel and Y. Zhang, Journal of Statistical Mechanics: Theory and Experiment **2022**, 113101 (2022).

[68] M. G. A. Paris, F. Illuminati, A. Serafini, and S. De Siena, Phys. Rev. A **68**, 012314 (2003).

[69] For certain values of N additional stable solutions appeared in less than 0.01% of the runs. These solutions were discarded as they would correspond to weakly stable minima occupying a very small volume in coordinate space, and thus unlikely to confine the objects under the influence of small – e.g. thermal – fluctuations.

[70] D. F. V. James, Applied Physics B **66**, 181 (1998).